



## How Well Do Multisatellite Products Capture the Space–Time Dynamics of Precipitation? Part I: Five Products Assessed via a Wavenumber–Frequency Decomposition

CLEMENT GUILLOTEAU,<sup>a</sup> EFI FOUFOULA-GEORGIU,<sup>a,b</sup> PIERRE KIRSTETTER,<sup>c,d</sup> JACKSON TAN,<sup>c,f</sup> AND  
GEORGE J. HUFFMAN<sup>e</sup>

<sup>a</sup> *Department of Civil and Environmental Engineering, University of California, Irvine, Irvine, California*

<sup>b</sup> *Department of Earth System Science, University of California, Irvine, Irvine, California*

<sup>c</sup> *Hydrometeorology and Remote Sensing Laboratory, University of Oklahoma, Norman, Oklahoma*

<sup>d</sup> *NOAA/Severe Storms Laboratory, Norman, Oklahoma*

<sup>e</sup> *NASA Goddard Space Flight Center, Greenbelt, Maryland*

<sup>f</sup> *Universities Space Research Association, Columbia, Maryland*

(Manuscript received 13 April 2021, in final form 20 July 2021)

**ABSTRACT:** As more global satellite-derived precipitation products become available, it is imperative to evaluate them more carefully for providing guidance as to how well precipitation space–time features are captured for use in hydrologic modeling, climate studies, and other applications. Here we propose a space–time Fourier spectral analysis and define a suite of metrics that evaluate the spatial organization of storm systems, the propagation speed and direction of precipitation features, and the space–time scales at which a satellite product reproduces the variability of a reference “ground-truth” product (“effective resolution”). We demonstrate how the methodology relates to our physical intuition using the case study of a storm system with rich space–time structure. We then evaluate five high-resolution multisatellite products (CMORPH, GSMaP, IMERG-Early, IMERG-Final, and PERSIANN-CCS) over a period of 2 years over the southeastern United States. All five satellite products show generally consistent space–time power spectral density when compared to a reference ground gauge–radar dataset (GV-MRMS), revealing agreement in terms of average morphology and dynamics of precipitation systems. However, a deficit of spectral power at wavelengths shorter than 200 km and periods shorter than 4 h reveals that all satellite products are excessively “smooth.” The products also show low levels of spectral coherence with the gauge–radar reference at these fine scales, revealing discrepancies in capturing the location and timing of precipitation features. From the space–time spectral coherence, the IMERG-Final product shows superior ability in resolving the space–time dynamics of precipitation down to 200-km and 4-h scales compared to the other products.

**SIGNIFICANCE STATEMENT:** Precipitation estimation products are essential for understanding water cycle dynamics and climate change, and for decision support in regions lacking ground observations. Several global products exist from multiple satellites orbiting Earth, but the challenge remains that of evaluating these products for accuracy and for improving the retrieval algorithms. Here we posit that the classical “pixel-to-pixel” comparison is not adequate and propose an approach that focuses on comparing space–time dynamics through a Fourier spectral analysis, which provides information about the size, shape, and orientation of precipitation systems, as well as their motion speed and direction. We evaluate five state-of-the-art multisatellite products and identify shortcomings, in particular in their ability to capture the submesoscale variability of precipitation.

**KEYWORDS:** Precipitation; Error analysis; Remote sensing; Satellite observations; Radars/Radar observations; Fourier analysis; Spectral analysis/models/distribution

### 1. Introduction

Satellite-derived quantitative precipitation estimation (QPE) products have been around for several decades and are now commonly used in climate studies (Mehta and Yang 2008; Roca et al. 2014; Kerns and Chen 2020), hydrologic modeling and prediction (Casse and Gosset 2015), and various other applications (Kirschbaum et al. 2017), including vegetation monitoring (Hilker et al. 2014; Suepa et al. 2016), landslide risk management (Kirschbaum and Stanley 2018), health risk management (Guilloteau et al. 2014), etc. Extensive literature exists on

Denotes content that is immediately available upon publication as open access.

Supplemental information related to this paper is available at the Journals Online website: <https://doi.org/10.1175/JHM-D-21-0075.s1>.

Corresponding author: Clement Guilloteau, [cguillot@uci.edu](mailto:cguillot@uci.edu)

DOI: 10.1175/JHM-D-21-0075.1

© 2021 American Meteorological Society. For information regarding reuse of this content and general copyright information, consult the [AMS Copyright Policy](#) ([www.ametsoc.org/PUBSReuseLicenses](http://www.ametsoc.org/PUBSReuseLicenses)).

evaluating and validating satellite products (e.g., Sapiano and Arkin 2009; Derin et al. 2016; Beck et al. 2019). In all of these evaluation or validation efforts, the satellite products must be compared with a “truth,” typically a ground reference measurement, such as from rain gauges or ground precipitation radars.

Precipitation exhibits spatial and temporal variability across a wide range of scales ranging from the microscale (subkilometric, subhourly) to the synoptic and multidecadal scales. This variability includes specific spatiotemporal modes corresponding to regular features which may be periodic such as the diurnal cycle, seasonal cycle, intraseasonal cycles (e.g., due to the Madden–Julian oscillation), interannual cycles (e.g., due to El Niño–Southern Oscillation), or potentially long-term trends (e.g., effects of anthropogenic aerosols and greenhouse gas emissions). These regular modes of precipitation variability coexist and interact with less predictable chaotic variability, resulting in complex regional and local patterns of precipitation. An important question about satellite QPEs is how well the space–time dynamics of precipitation are captured across a range of scales relevant for hydrologic applications and decision support.

The classical approach for comparing a QPE to a reference measurement is to gather a set of coincident samples, i.e., individual estimates, each one corresponding to a given time and location, and compute sample statistics such as correlations, mean squared differences, detection rate, false alarm rate, etc. With this approach, which focuses on point or “pixel” statistics, each sample is considered independently and the fact that precipitation is a spatially and temporally correlated variable is ignored. As such, the classical scoring metrics do not inform us on the ability of QPE products to accurately capture the spatial and temporal *patterns* of precipitation. The interpretation of point or pixel sample statistics is always ambiguous for spatially and temporally correlated variables and the analysis of the sample statistics gives little insight about the nature of the retrieval errors, which could be additive or multiplicative random noise, but also systematic or random errors on the location and timing of the precipitation features, spatial and temporal distortion of the precipitation features, etc. Finally, from sample statistics computed at one given scale only, one cannot infer the performance of a precipitation product at any other scale. An alternative evaluation approach is object-based analysis, where a continuous precipitation area (above a given threshold) is defined as an object (e.g., Ebert and McBride 2000; Demaria et al. 2011, Tapiador et al. 2019; Li et al. 2020; Ayat et al. 2021). This approach allows to partially circumvent the abovementioned limitations. However, these types of methods are generally parametric (one important parameter being the intensity threshold chosen to define an object), and the results may be highly sensitive to the definition of the objects. As such, these methods are not easily applicable to large datasets without human supervision, and the results of studies performed with different parametric and methodological choices are not easily comparable. Additionally, complex mechanisms such as object splitting and merging over time may make the object-related statistics delicate to interpret.

Spectral representations such as the Fourier transform or wavelet transform are designated tools to analyze the dynamics of spatiotemporal variables (Yiou et al. 1996; Kyriakidis and Journel 1999; Oreopoulos et al. 2000; Harris et al. 2001;

Ghil et al. 2002). In particular, using a multidimensional space–time spectral analysis allows one to consider jointly spatial and temporal dynamics. Unlike the sample statistics, the space–time Fourier spectral analysis provides information on the size and lifetime of the precipitation systems/features; the potential spatial anisotropy of precipitation fields, including propagation effects with preferred directionality and propagation speed; and statistics on the dynamical modes of variability of precipitation, such as the diurnal and seasonal cycles or the response to atmospheric pressure waves (from small-scale internal gravity waves to synoptic Kelvin and Rossby waves). Fourier space–time spectral analysis has been used in climate science for several decades to identify modes of variability and evaluate model dynamics (Kao and Wendell 1970; Hayashi 1982; Wheeler and Kiladis 1999; Céron and Guérémy 1999; Orbe et al. 2020). It has also been used to investigate dynamical scaling in precipitation (Rysman et al. 2013) and sometimes to parameterize stochastic representations of rainfall (Kundu and Bell 2003; De Michele and Bernardara 2005). However, it has rarely been used to evaluate and compare observational datasets. The evaluation of the dynamical aspects of precipitation is particularly relevant to multisatellite QPEs as the spatiotemporal sampling allowed by a constellation of satellites on different orbits is itself highly dynamical, and the interpolation methods used to estimate precipitation between the observations often rely on dynamical constraints.

In the present study, five satellite QPEs, namely, CMORPH, GSMaP, IMERG-Early, IMERG-Final, and PERSIANN-CCS (see section 2 for detailed information and acronyms) are evaluated against NOAA’s gauge–radar Ground Validation Multi-Radar Multi-Sensor (GV-MRMS) product over the southeastern United States at scales down to 10 km and 1 h through (cross-) spectral space–time analysis relying on a three-dimensional fast Fourier transform (FFT). The three dimensions of the analysis are the two spatial dimensions (north–south and east–west directions) and the temporal dimension. The marginal (single variable) and joint distributions of the spectral power of the precipitation signal as a function of temporal frequency and spatial wavenumbers, revealed by the power spectral density (PSD), allows us to verify the scales at which the products have realistic spatiotemporal dynamics. Additionally, the spectral coherence between the satellite QPEs and the ground reference allows us to determine the scales at which the satellite can accurately reproduce the space–time dynamics of precipitation, as observed by the gauge–radar network, with concordant timing and location of the precipitation features. In Guilloteau et al. (2017) and Guilloteau and Foufoula-Georgiou (2020) the concept of spatial “effective resolution” of a product was introduced based on the spatial wavelet coherence between the evaluated product and reference gauge–radar fields. Here, this concept is extended to the spatial and temporal dimensions simultaneously.

The article is organized as follows. Section 2 presents the datasets and the study area and briefly introduces the spectral analysis method. Section 3 presents a case study of spectral analysis applied to a storm system to gain insight on the interpretation of the proposed metrics. Section 4 presents the results from the analysis of all data over a 2-yr period as a comparison of the spectral properties of the GV-MRMS

reference dataset with those of the satellite QPEs. In section 5 the spectral performance of an idealized gauge network is presented to quantify the gauge density necessary to achieve performance similar to the satellite retrievals and thus assess the “equivalent gauge value” of the satellite products. Section 6 presents a discussion on the effect of different retrieval methods and algorithms on the spectral properties of the retrieved precipitation fields. The dilemma of preserving the true space–time power spectrum of precipitation versus minimizing the mean squared retrieval error is discussed in this section. Section 7 presents the concluding remarks.

## 2. Data and methods

### a. GV-MRMS gauge–radar data

The half-hourly gauge–radar QPE from the Ground Validation Multi-Radar Multi-Sensor (GV-MRMS; Petersen et al. 2020) suite of products is used in this study as a high-quality reference to evaluate the satellite QPEs. GV-MRMS builds on the MRMS QPE that is derived from 176 WSR-88D radars and more than 18 000 automatic hourly rain gauges over the contiguous United States and Canada (Zhang et al. 2016). Advanced data integration techniques are used to create 3D reflectivity mosaic grids and quantitative precipitation estimates blending radar and gauge data at the necessary resolution for the evaluation of satellite QPEs. Less trustworthy GV-MRMS estimates are filtered using a radar quality index and gauge-based quality control. These procedures are necessary to obtain a high-quality and standardized reference across the study domain for satellite evaluation purposes (Kirstetter et al. 2012, 2020). The half-hourly precipitation estimates are produced on a regular grid with  $0.01^\circ$  latitude and longitude increments. The southeastern part of the United States between the latitudes  $30^\circ$  and  $41^\circ\text{N}$  and between longitudes  $81^\circ$  and  $102^\circ\text{W}$  (Fig. 1), over which the radar coverage is excellent (49 radars cover this 2.3 million  $\text{km}^2$  area), as well as excellent gauge coverage, is selected as a benchmark area for evaluating the satellite QPEs. We consider here that the errors of the GV-MRMS estimation at the 10-km hourly resolution at which our analysis is performed are negligible compared to the errors in the satellite QPEs. The ability of the gauge–radar product to capture the fine-scale variability of precipitation is trusted in particular because of the high instrumental resolution and sampling frequency of the radars. The GV-MRMS dataset provides the spatial and temporal continuity required to study the spatiotemporal structure of precipitation fields.

### b. Multisatellite precipitation products

Five multisatellite precipitation products are evaluated in the present study. All of them are quasi-global products, covering all longitudes and the latitudes between  $60^\circ\text{N}$  and  $60^\circ\text{S}$ . All five products offer an hourly or higher temporal sampling and provide precipitation estimates on a grid with a latitude/longitude increment equal to or finer than  $0.1^\circ$ . They are all publicly available for research purposes.

The PERSIANN-CCS (Precipitation Estimation from Remotely Sensed Information using Artificial Neural Networks–Cloud

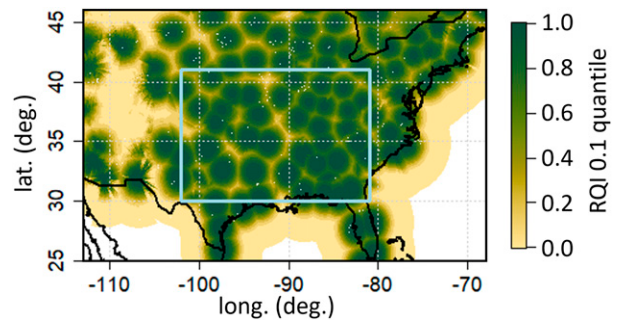


FIG. 1. Map of the lower 10th percentile of MRMS radar quality index over the contiguous United States. The blue rectangle corresponds to the study area. The quality index takes into account the distance to the closest radar, the altitude of the freezing level, and beam blockage by the relief [see Zhang et al. (2016) for precise definition]. We show here the lower 10th percentile, meaning that the quality index is higher than the shown value 90% of the time.

Classification System; Hong et al. 2004), derives precipitation estimates from the longwave thermal infrared channel (wavelength between 10 and  $12.5\ \mu\text{m}$ ) of imagers on geostationary orbits. The area considered in this study was monitored by the Advanced Baseline Imager (ABI) on board the *GOES-16* satellite during the 2018–20 study period. The algorithm first performs a cloud classification based on texture parameters. A relation between the infrared brightness temperature and the precipitation intensity, specific to each cloud class, is then used to estimate half-hourly accumulated precipitation. PERSIANN-CCS is produced by the Center for Hydrometeorology and Remote Sensing of the University of California, Irvine.

GSMaP-MVK (Global Satellite Mapping of Precipitation–Moving Vector with Kalman filter; Ushio et al. 2009) has been developed by the Japan Aerospace Exploration Agency (JAXA) as part of the Tropical Rainfall Measuring Mission (TRMM; Kummerow et al. 2000) and Global Precipitation Measurement (GPM) mission (Hou et al. 2014) international programs. It relies on the estimation of precipitation rates from about a dozen multispectral microwave imagers and sounders on low-Earth orbits. To fill the gaps between the satellite overpasses, a dynamic interpolation is performed relying on cloud motion vectors derived from geostationary infrared (Geo-IR) imagery and Kalman filtering. Version 7 of the product is used in the present study.

The CPC morphing technique (CMORPH; Joyce et al. 2004; Joyce and Xie 2011; Xie et al. 2017) produced by the U.S. National Oceanic and Atmospheric Administration (NOAA) Climate Prediction Center, is similar in concept to GSMaP. It relies on a similar constellation of microwave imagers and sounders (most of them being common with those used for the GSMaP algorithm), and also implements a Kalman filter interpolation approach with Geo-IR-derived cloud motion vectors. CMORPH and GSMaP differ by the microwave retrieval schemes used for estimating precipitation rates and the parameterization of the Kalman filter. For version 1.0 of the CMORPH product, used in the present study, the quantitative biases of CMORPH over land are corrected locally with correction parameters estimated from the climatology of the CPC gauge analysis product over 30-calendar-day periods.

The Integrated Multisatellite Retrievals for GPM (IMERG; Huffman et al. 2019) product has been developed by the U.S. National Aeronautics and Space Administration (NASA) as part of the GPM international program. It relies on the GPM international constellation of low-Earth-orbit microwave imagers and sounders (Hou et al. 2014) and on Geo-IR. It implements a CMORPH-like motion vector method to dynamically interpolate the microwave-derived precipitation rates, though in Version 06, used in the present study, the motion vectors are computed from the total precipitable water vapor field of numerical models instead of Geo-IR (Tan et al. 2019). IMERG additionally assimilates the infrared precipitation rates from the PERSIANN-CCS algorithm as part of the Kalman filtering process. Three different IMERG products are made available with different latency: the “Early” product (IMERG-E) is available 4 h after observation times, the “Late” (IMERG-L) is available 14 h after observation and the “Final” product (IMERG-F) is available 4 months later. IMERG-E implements a one-way Kalman filter approach while IMERG-L and IMERG-F rely on a two-way Kalman smoother (i.e., dynamical interpolation from both “past” and “future” observations at estimation time). The Late and Final products also assimilate a higher number of microwave observations than the Early product as all microwave observations are not always available with the 4-h latency. The “uncalibrated” precipitation estimates that do not include gauge adjustment from IMERG-E and IMERG-F products are used in the present study.

The January 2018–April 2020 period is selected for the evaluation of the satellite products. The March 2018 and March 2019 months are excluded from the analysis because of a high rate of missing MRMS data (or data not meeting the high GV quality standard) for this period. As the Fourier transform does not accommodate discontinuous data in space and time, all gaps in the data must be interpolated; in the present article a linear temporal interpolation is used for missing data when the gap is shorter than 2 h. The native space–time grid sampling of CMORPH, GSMaP, IMERG, and PERSIANN-CCS are, respectively,  $0.08^\circ \times 0.08^\circ \times 30 \text{ min}$ ,  $0.1^\circ \times 0.1^\circ \times 60 \text{ min}$ ,  $0.1^\circ \times 0.1^\circ \times 30 \text{ min}$ , and  $0.04^\circ \times 0.04^\circ \times 60 \text{ min}$ .

### c. Space–time Fourier spectral analysis

Our space–time spectral analysis relies on a three-dimensional Fourier transform. If  $g(x, y, t)$  is a function of space and time, for example, an estimate of precipitation intensity, its Fourier transform is defined as

$$\hat{g}(k_x, k_y, f) = \iiint_{-\infty}^{+\infty} g(x, y, t) e^{-i2\pi(k_x x + k_y y + ft)} dx dy dt, \quad (1)$$

with  $k_x$  and  $k_y$  the spatial wavenumbers and  $f$  the temporal frequency. The Fourier power spectral density (PSD) of  $g(x, y, t)$  is defined as

$$P_g(k_x, k_y, f) = \hat{g}(k_x, k_y, f) \times \hat{g}^*(k_x, k_y, f), \quad (2)$$

with the operator  $*$  denoting the complex conjugate. The Fourier power cross-spectral density (PCSD) between two

functions  $g(x, y, t)$  and  $h(x, y, t)$ , for example, two different estimates of precipitation intensity, is defined as

$$P_{gh}(k_x, k_y, f) = \hat{g}(k_x, k_y, f) \hat{h}^*(k_x, k_y, f). \quad (3)$$

In practice, for finite-length datasets, a discrete FFT is used and local averaging in the Fourier frequency–wavenumber domain is necessary to obtain robust estimates of the PSD and PCSD (Proakis and Manolakis 2001). The PSD reveals how the analyzed signal can be decomposed as a sum of oscillations (waves) and how much energy is associated with these waves as a function of the wavenumber (number of oscillations per unit of space) and the frequency (number of oscillations per unit of time). The PCSD indicates whether the oscillations contained in two different signals synchronize or not and how much common energy they have. We use here the term “energy” in the statistical sense, meaning the integral value over space and time of the square of a variable (here precipitation rate); it is not directly related to the physical energy (in the thermodynamics sense) of the atmospheric systems. Power is defined as energy per unit of time/space. The space–time PSD and PCSD are uniquely related to the space–time autocorrelation and cross-correlation functions through the Wiener–Khinchin theorem (Cohen 1998).

The Fourier spectral coherence between  $g(x, y, t)$  and  $h(x, y, t)$  is defined as

$$C_{gh}(k_x, k_y, f) = \frac{P_{gh}(k_x, k_y, f)}{\sqrt{P_g(k_x, k_y, f) \times P_h(k_x, k_y, f)}}. \quad (4)$$

The spectral coherence is a complex number with a modulus between 0 and 1. It can be interpreted as the complex correlation of the Fourier coefficients within narrow frequency/wavenumber bands. The phase (argument) of the spectral coherence gives the average phase shift between the two variables in each frequency/wavenumber band. A null spectral coherence indicates unsynchronized oscillations with a randomly varying instantaneous phase shift between the two signals at the corresponding periods and wavelengths. A spectral coherence with a unit modulus indicates identical oscillating signals (up to a multiplicative constant and a constant phase shift) at the corresponding period and wavelength.

The PSD and the spectral coherence being quadratic measures, they are strongly influenced by the extreme values in the signal. One can analyze the space–time dynamics of precipitation with regard to a specific precipitation intensity value (or a specific quantile) by thresholding the precipitation fields in order to obtain a binary variable before performing the spectral analysis (not done here). Alternatively, one could perform the spectral analysis on the quantile fields, i.e., on the intensity values mapped to a uniform distribution. The classical sample statistics, mean squared difference (MSD), and Pearson correlation coefficient (CC) can be derived from the power spectral and cross-spectral densities:

$$\text{MSD}_{gh} = \iint_{-\infty}^{+\infty} [P_g + P_h - 2\text{Re}(P_{gh})] dk_x dk_y df \quad (5)$$

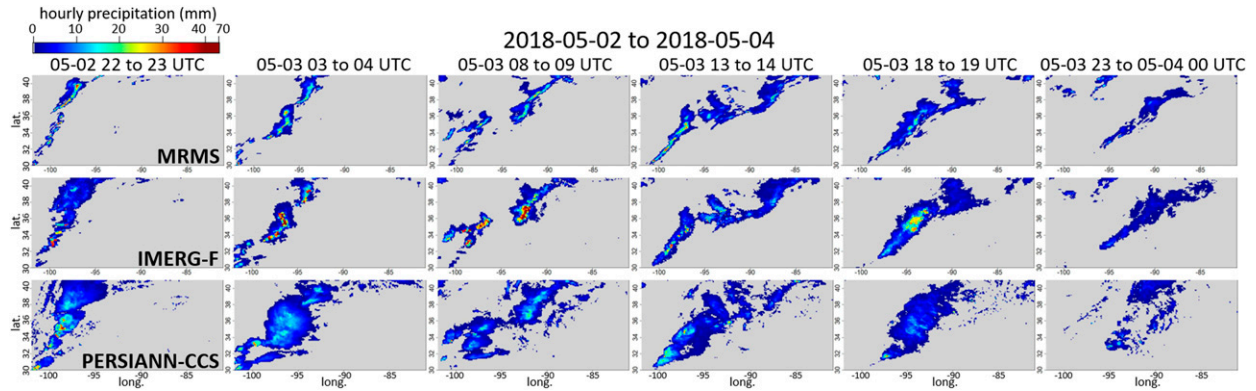


FIG. 2. A case study storm system, as retrieved on 2–4 May 2018 by GV-MRMS, IMERG-F, and PERSIANN-CCS over the south-eastern United States. The images correspond to discontinuous snapshots of hourly accumulated precipitation. An animated version of this figure is provided in the online supplemental material. The estimates of the area-averaged cumulated precipitations for this storm are 19, 29, and 33 mm for MRMS, IMERG-F, and PERSIANN-CCS, respectively.

$$\begin{aligned}
 CC_{gh} = & \left( \iint \int_0^{+\infty} \text{Re}(P_{gh}) dk_x dk_y df \right. \\
 & \times \left. \left( \iint \int_0^{+\infty} P_g dk_x dk_y df \times \iint \int_0^{+\infty} P_h dk_x dk_y df \right)^{-1/2} \right) \quad (6)
 \end{aligned}$$

where  $\text{Re}(P_{gh})$  is the real part of  $P_{gh}$ .

Because of the difficulty in visually representing functions of three variables, in the present article, we show the marginal PSDs as well the joint PSDs along two of the three dimensions. The marginal PSD along one dimension is obtained by integrating the three-dimensional PSD along the other two dimensions. Similarly, the joint PSD along two dimensions is obtained by integrating the three-dimensional PSD along the third dimension. In the following, spectral quantities are interpreted as functions of temporal period and spatial wavelengths rather than frequency and wavenumbers; wavelength and period are the inverse of wavenumber and frequency respectively.

Before applying the Fourier transform, the GV-MRMS and satellite QPEs are projected (and interpolated when necessary) on a common  $0.1^\circ \times 0.1^\circ \times 30$  min latitude/longitude/time grid. The 30-min temporal sampling is used for better spectral resolution but the temporal periods shorter than 2 h are excluded from the analysis after the Fourier transform to avoid penalizing GSMaP and PERSIANN-CCS, which have an hourly native sampling. The spatial wavelengths are shown in kilometers, which is converted from degrees latitude/longitude using the following conversion ratio for the study region:  $1^\circ$  latitude corresponds to approximately 110 km while  $1^\circ$  longitude corresponds to approximately 90 km.

### 3. A case study for the interpretation of spectral quantities for storm diagnostics

In this section we demonstrate the methodology on a specific storm system to gain physical insight on the results (before applying it to an ensemble of storms over a period of 2 years in the next section). Specifically, through the comparison of the satellite and gauge–radar space–time PSDs as well as the

analysis of their relative spectral coherence, we evaluate how well satellite-derived products reproduce precipitation features across space–time scales, such as: 1) the *morphology and orientation* of the storm system, 2) the *dynamics and propagative features (speed and direction)*, and 3) *consistency of precipitation features’ location and timing*.

Since the analysis is performed over a range of scales, we can assess the space–time scales at which precipitation variability is adequately represented in the products (“effective space–time resolution”). In this case study, we perform the space–time spectral analysis of GV-MRMS, IMERG-F and PERSIANN-CCS precipitation fields over the study area for a 2-day period (1900 UTC 2 May 2018–0800 UTC 4 May 2018) during which a frontal mesoscale convective storm system with several squall lines propagated from west to east (see the evolution of the system as captured by GV-MRMS, IMERG-F, and PERSIANN-CCS on Fig. 2 and in the animation provided as online supplemental material).

The PSDs resulting from the three-dimensional Fourier transform are shown on Fig. 3. We first analyze the joint PSDs along the two spatial dimensions (Fig. 3, left column). Passing into the polar coordinate system through the change of variable  $k = \sqrt{k_x^2 + k_y^2}$  and  $\theta = \text{atan}(k_x/k_y)$ , we can assess the dependence of the PSD on the azimuthal direction  $\theta$ . Here,  $\theta$  is defined as the angle clockwise from the north, following the traditional compass convention. For the GV-MRMS and the two satellite products, the two-dimensional spatial PSD exhibits a preferred directionality, revealing the anisotropy of the precipitation fields. Specifically, the PSD is higher in the directions between  $290^\circ$  and  $330^\circ$  than in the other directions; this direction is the direction of the strongest gradients in the precipitation, i.e., the direction orthogonal to the squall lines. The anisotropy is particularly pronounced for GV-MRMS, for which it affects all wavelengths down to the 20-km wavelength. For IMERG-F the anisotropy is strong at long wavelengths but fades progressively at wavelengths shorter than 100 km, revealing that IMERG-F only shows pronounced directionality for the precipitation features of dimension larger than  $\sim 100$  km. For PERSIANN-CCS the

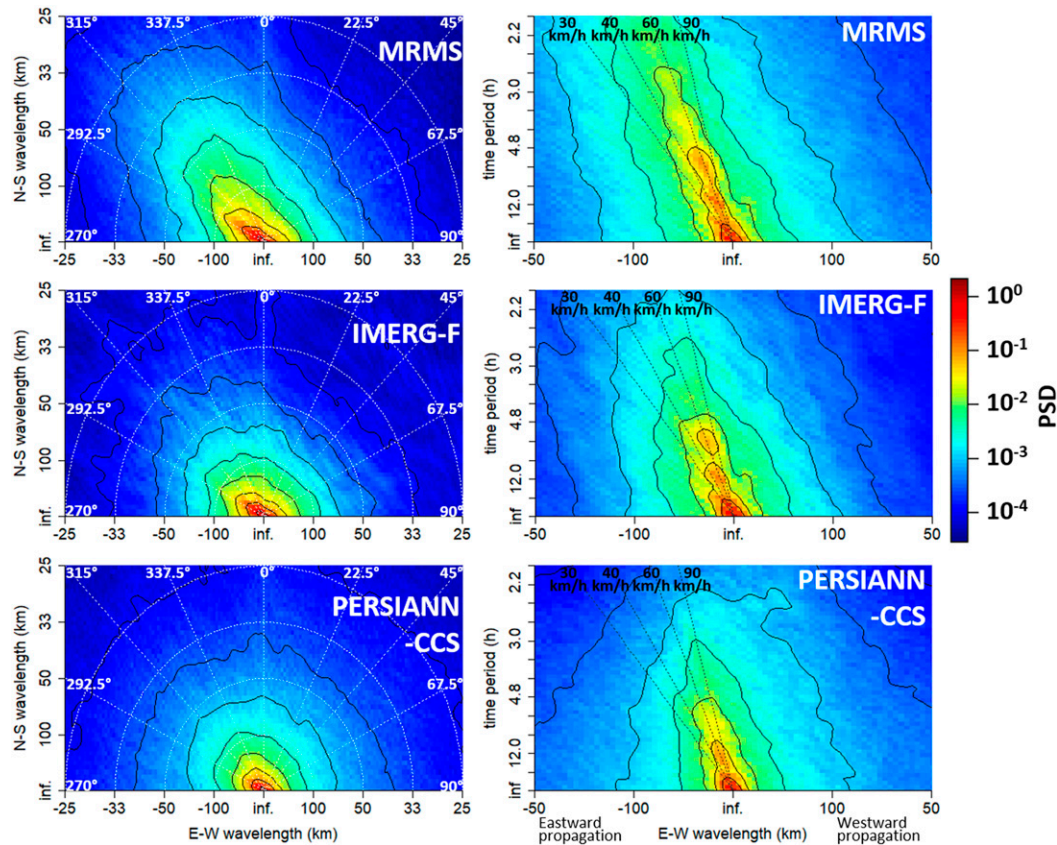


FIG. 3. Morphology and dynamics of the storm system in Fig. 2 as revealed by the PSD. (left) Joint PSDs of GV-MRMS, IMERG, and PERSIANN-CCS computed over the southeastern United States from 1900 UTC 2 May 2018 to 0800 UTC 4 May 2018 along the east–west and north–south spatial dimensions, and (right) along the east–west spatial dimension and the temporal dimension. In the left panels, higher spectral power is found in the  $290^{\circ}$  to  $330^{\circ}$  direction (northwest), which is the direction of the strongest gradients. In the right panels, most of the spectral power is associated with negative wavelengths (eastward propagation); the spectral power is concentrated along the lines corresponding to  $40\text{--}90\text{ km h}^{-1}$  velocity. In all panels, smoothed isocontours are added at  $10^0$ ,  $10^{-1}$ ,  $10^{-2}$ ,  $10^{-3}$ , and  $10^{-4}$  for enhanced visualization.

anisotropy is only salient at wavelengths longer than 200 km. These differences in the PSD are related to the different morphology of the storm across the three products (Fig. 2). GV-MRMS shows a well-defined frontal system with a narrow convective front forming thin lines in the southwest–northeast direction. While IMERG-F captures well the general shape and orientation of the frontal storm system, the convective areas in the IMERG-F fields are thicker and less elongated than in the GV-MRMS fields. The general shape of the system is less elongated in the PERSIANN-CCS product which tends to produce elliptic precipitation areas with relatively low eccentricity.

The joint space–time PSDs are only shown for the east–west direction (Fig. 3, right column). Two-dimensional space–time PSDs are commonly used in climate and Earth science to analyze the propagation of atmospheric and oceanic waves along longitudes (Wheeler and Kiladis 1999; Lin et al. 2006; Orbe et al. 2020). The left half of the PSD (negative wavelengths) corresponds to eastward propagating waves and the right half

(positive wavelengths) corresponds to westward propagating waves. The two-dimensional space–time PSD shows the energy of the eastward and westward propagating waves as a function of their spatial wavelength and temporal period. The ratio between wavelength and period defines the phase propagation velocity of the waves. A linear relationship between wavelength and period indicates nondispersive wave propagation (i.e., a phase velocity independent of the wavelength). For the present case study, the eastward propagation of the storm system appears neatly in the PSD, with most of the spectral power associated with the negative wavelengths. The propagation speed of the system is also revealed by the space–time PSD, with the spectral power concentrated along the lines corresponding to  $40\text{--}90\text{ km h}^{-1}$  velocity. GV-MRMS shows more spectral power than IMERG-F and PERSIANN-CCS at temporal periods shorter than 4 h and wavelengths shorter than 200 km.

The spectral coherence (modulus) between GV-MRMS and the satellite products (Fig. 4) allows us to evaluate the ability of

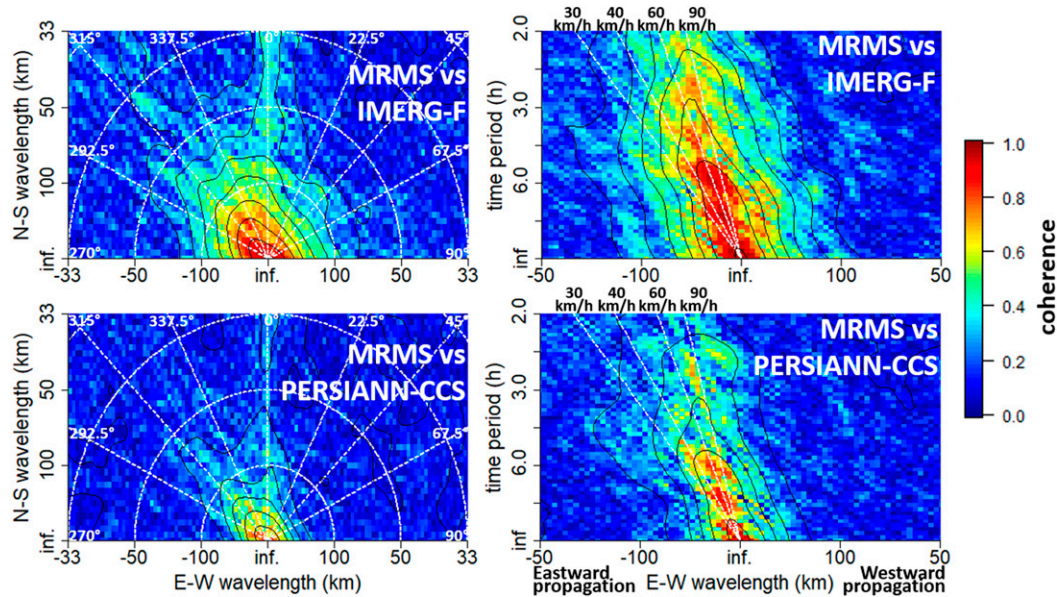


FIG. 4. Consistency between GV-MRMS and the satellite products in terms of timing and location of the precipitation features as functions of spatial wavelengths and temporal period revealed by the spectral coherence for the storm system in Fig. 2. Spectral coherence (modulus) between GV-MRMS and IMERG and between GV-MRMS and PERSIANN-CCS computed over the southeastern United States from 1900 UTC 2 May 2018 to 0800 UTC 4 May 2018, (left) as a function of east–west and north–south spatial wavelengths and (right) as a function of the east–west spatial wavelength and of the temporal period. IMERG-F accurately captures the gradients in the directions between 290° and 320° down to the 50-km wavelength and the features propagating with a velocity around 60 km h<sup>-1</sup> down to the 2-h time period. PERSIANN-CCS only accurately captures the spatial dynamics down to the 100-km wavelength and down to the 4 h time period. In all panels, smoothed isocontours are added at 0.1, 0.2, . . . , and 0.9 for enhanced visualization.

IMERG-F and PERSIANN-CCS to capture precipitation features with the right timing and location as functions of spatial wavenumber (wavelength), temporal frequency (period), directionality of the spatial gradients, propagation speed and propagation direction of the features. In this case study, it appears that PERSIANN-CCS only captures accurately the spatial gradients down to the 100-km wavelength and the temporal dynamics down to the 4-h time period, at finer space–time scales, the coherence with GV-MRMS is not statistically significant (at the 0.01 level). IMERG-F captures accurately the gradients down to the 50-km wavelength and the temporal dynamics down to the 2-h time period. The dominant features propagating eastward with a 40–90 km h<sup>-1</sup> velocity are the ones for which the spectral coherence with GV-MRMS is the highest for both IMERG-F and PERSIANN-CCS, revealing that the satellite products capture well the dominant propagative features, but not so well the secondary or local propagative patterns.

We note that the total precipitation associated with the storm system presented in this case study is overestimated by a factor of 1.5 in IMERG-F and by a factor of 1.8 in PERSIANN-CCS compared to the GV-MRMS reference estimate, with area-averaged cumulated precipitations of 19, 29, and 33 mm for MRMS, IMERG-F, and PERSIANN-CCS respectively. However, one should note that constant multiplicative biases do not affect the spectral coherence or the shape of the PSD

function. In the present article, all PSDs shown are normalized by the PSDs at the zero frequency and zero wavenumbers, i.e., the power associated with the mean value of the signal (the DC, or “direct current,” component in signal processing terminology).

#### 4. Comparison of five multisatellite products from 2 years of data

The performance evaluation consists of the comparison of the PSD of the satellite QPEs with the PSD of GV-MRMS and the analysis of the spectral coherence between the satellite QPEs and GV-MRMS as functions of spatial wavenumber (wavelength), temporal frequency (period), directionality of the spatial gradients, propagation speed and propagation direction of the features. One advantage of the spectral approach, as compared for example to object-based approaches, is that one can compute spectra over a long time period and a large area and extract the average characteristics of storm systems without having to identify each storm individually.

##### a. Marginal PSDs: Spatial and temporal variability assessed independently

Figure 5 (top) shows the marginal PSDs along time and the two spatial dimensions. All products show a peak corresponding to the diurnal cycle of precipitation at the one-day

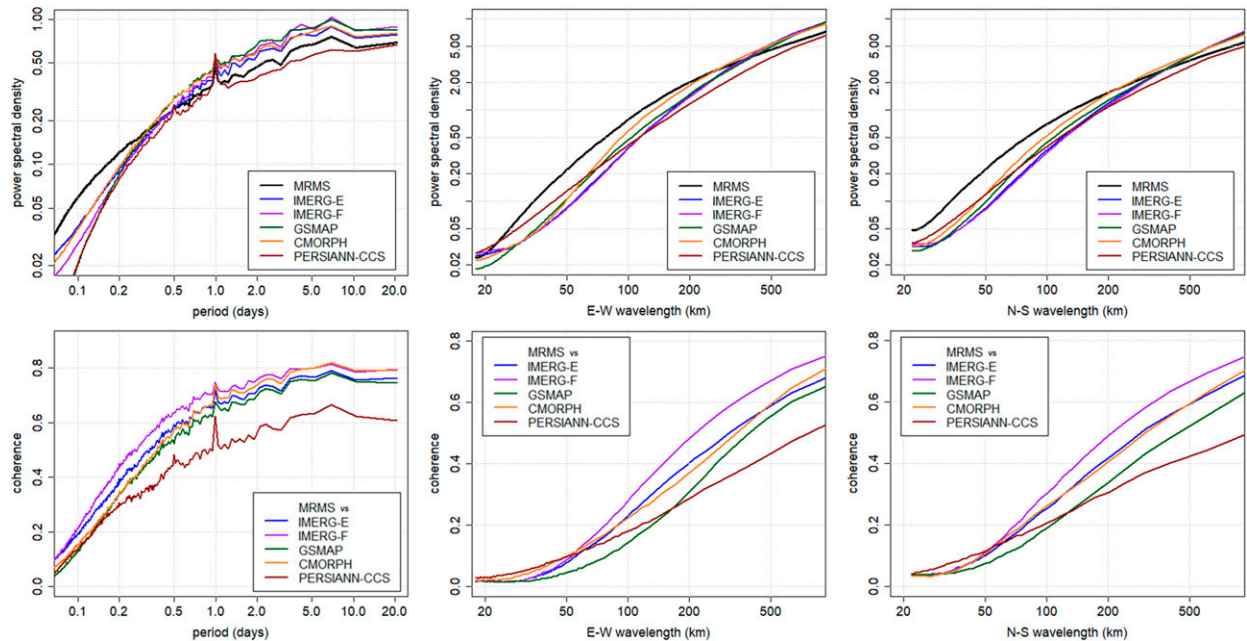


FIG. 5. Temporal and spatial dynamics of precipitation over the southeastern United States as revealed by the marginal PSDs and consistency of the satellite products with GV-MRMS as revealed by the spectral coherence. (top) Marginal (left) temporal and (center),(right) spatial longitudinal and latitudinal PSDs of GV-MRMS and satellite precipitation fields from 2018 to 2020. (bottom) Spectral coherence (modulus) between the GV-MRMS and satellite precipitation fields as functions of (left) temporal period and (center),(right) spatial wavelengths. The PSD increasing with longer periods/wavelengths indicates spatially and temporally correlated features with correlation decreasing with time delay and distance. In the left panels, the peak at the 1-day period corresponds to the diurnal cycle. IMERG-F show the highest temporal coherence at all frequencies and highest spatial coherence at wavelengths greater than 70 km.

period and the 0.5 days harmonic (indicating that the diurnal cycle is not perfectly sinusoidal) is also visible in the PERSIANN-CCS spectrum. While the shape and timing of the diurnal cycle varies across the study region, the PERSIANN family products generally have a pronounced diurnal cycle with a narrow single peak in the afternoon (Dai et al. 2007; Nguyen et al. 2020). Beside this peak for the diurnal cycle all spectra show decreasing PSD with shorter periods and wavelengths, reflecting the well-known fact that precipitation is a spatially and temporally correlated variable with correlation decreasing at longer distances and greater temporal delays (Zawadzki 1973; Waymire and Gupta 1981). It is, however, worth noting that neither the temporal power spectra nor the spatial spectra appear linear in the log–log scale. The approximation of the temporal or spatial marginal PSD by a power law of the form  $P(f) = \alpha f^\beta$ , or respectively  $P(k) = \alpha k^\beta$ , (i.e., as a “warm color” power spectrum when  $\beta < 0$ ), which is often found in the literature for climate variables (Gilman et al. 1963; Lovejoy and Schertzer 1986; Harris et al. 2001; Tustison et al. 2001), would therefore be a poor approximation of the empirical PSDs in the present case. The GV-MRMS reference spectrum is the one showing the strongest deviation from log–log linearity for both temporal and spatial spectra.

For the temporal spectra, GV-MRMS and the satellite products show similar distributions of spectral power at periods ranging from 0.5 to 20 days. For time periods shorter than

0.5 days the satellite products show a significantly faster decay of the PSD with shorter periods than GV-MRMS. This means that the satellite products are temporally smoother, i.e., have higher short-term temporal correlation of the precipitation rates than GV-MRMS. For all products, the spatial spectra in the east–west and north–south directions are nearly identical. All satellite products significantly underestimate the spatial variability at wavelengths shorter than 300 km in both directions when compared to GV-MRMS, indicating excessive short-range spatial correlation in satellite precipitation. We note that the IMERG-E and IMERG-F spatial spectra are nearly identical while their temporal spectra diverge significantly at periods shorter than 6 h (IMERG-F showing lower PSD than IMERG-E at these high temporal frequencies).

In terms of spectral coherence between the satellite QPEs and GV-MRMS (Fig. 5, bottom), all products show a decrease of coherence with shorter periods and wavelengths, with the exception of the peak at the 1-day period. At all temporal periods and at wavelengths longer than 60 km, IMERG-F shows the highest coherence with GV-MRMS, implying that this product is the most consistent with GV-MRMS in terms of coincident spatial and temporal patterns. PERSIANN-CCS shows significantly lower coherence with GV-MRMS than the other satellite products at periods greater than 4 h and at wavelengths longer than 200 km. We note that for wavelengths longer than 50 km CMORPH and IMERG-E show very similar coherence with GV-MRMS. For all satellite products and at all

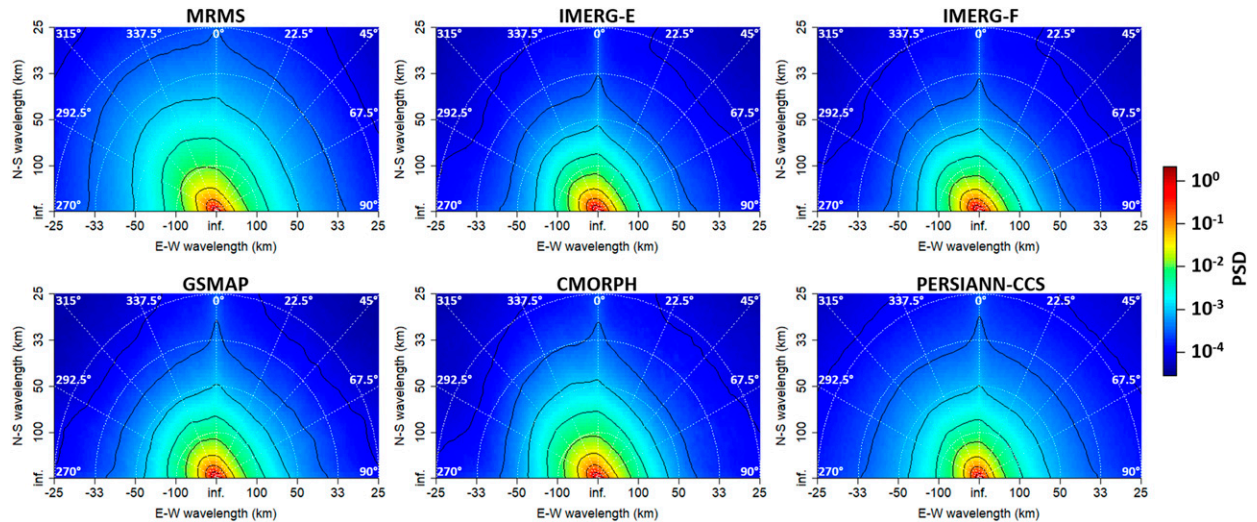


FIG. 6. Average morphology and orientation of precipitation systems over the southeastern United States as revealed by the 2D spatial PSD. Joint spatial PSDs of the GV-MRMS and satellite precipitation fields in the north–south and east–west directions. Higher spectral power is found around the  $320^\circ$  direction (approximately northwest), which is the direction of the strongest precipitation gradients. In all panels, smoothed isocontours are added at  $10^0$ ,  $10^{-1}$ ,  $10^{-2}$ ,  $10^{-3}$ , and  $10^{-4}$  for enhanced visualization.

wavelengths, the coherence with GV-MRMS in the north–south and east–west directions is also very similar.

#### b. Joint east–west and north–south spatial PSDs:

##### *Directional morphology of precipitation systems*

We now analyze the PSD as a function of the two east–west and north–south spatial dimensions (Fig. 6). The first noticeable characteristic is the circular asymmetry of the PSDs, with higher power density in the  $320^\circ$  azimuthal direction (approximately northwest–southeast). This reveals the spatial anisotropy of the precipitation fields; the strongest spatial gradients are found around the  $320^\circ$  direction while lower variability (higher spatial correlation) is found in the orthogonal direction ( $50^\circ$ , approximately southwest–northeast). This is consistent with the fact that most of the linear precipitation features such as squall lines are approximately oriented along the southwest–northeast direction in the southeastern United States (Newton 1950). It is worth noting that, because the preferred direction is neither north–south nor east–west but rather the “diagonal” direction, the anisotropy was not apparent from the marginal north–south and east–west PSDs (Fig. 5). This shows that computing the unidimensional spatial PSD (or variogram/autocovariance function) in only two orthogonal directions is generally not sufficient to detect anisotropy. We note that the small increase of the PSDs in the  $0^\circ$ ,  $90^\circ$ , and  $270^\circ$  directions is an artifact caused by the fact that the pixels are  $0.1^\circ \times 0.1^\circ$  squares. All the satellite QPEs reproduce the spatial anisotropy shown by GV-MRMS; we note however that the anisotropy appears less pronounced for PERSIANN-CCS than for the other products. We compute the average PSD as a function of the spatial direction by integrating the two-dimensional spatial PSD between wavelengths 20 and 300 km for each azimuthal angle  $\theta$  (Fig. 8, left panel). From this function  $\text{PSD}(\theta)$  we compute the anisotropy factor, which we

define as the ratio between the maximum and the minimum of  $\text{PSD}(\theta)$ . The anisotropy factors for GV-MRMS and each of the satellite products are listed in Table 1. PERSIANN-CCS has a lower anisotropy factor (2.1) than GV-MRMS (2.5) and the other satellite products (2.4–2.5). Another quantitative metric shown in Table 1 is the submeso power fraction. We also derive this metric from the two-dimensional spatial PSD; it is defined the fraction of the spectral power explained by the wavelengths shorter than 300 km. The submeso power fraction is found significantly lower for all the satellite products (45%–51%) than for GV-MRMS (62%), confirming the fact that the gauge–radar product shows higher fine-scale variability than the satellite products.

Comparing the five satellite products to GV-MRMS to assess how well they reproduce the precipitation spatial organization, with accurate localization of the spatial features, Fig. 7 shows the spectral coherence between GV-MRMS and the satellite QPEs as a function of the spatial north–south and east–west wavelengths. Figure 8 (right panel) shows the integrated coherence for wavelengths between 20 and 300 km as a function of the azimuthal angle. We note that the direction of maximal PSD is also the direction of maximal coherence for all the satellite products, except for PERSIANN-CCS, for which the maximum coherence with GV-MRMS is found in the north ( $0^\circ$ ) direction. Simple signal to noise ratio considerations can explain the fact that the stronger gradients in the southeast–northwest direction are better captured by the satellites: the higher magnitude of precipitation variability in this direction is expected to cause a higher-magnitude signal in the measured radiances in the same direction; in contrast, the magnitude of the noise in the measured radiances is expected to be the same in all directions. Higher signal to noise ratio, leading to better retrieved precipitation signal, is therefore expected in the direction of the stronger precipitation gradients. One shall note

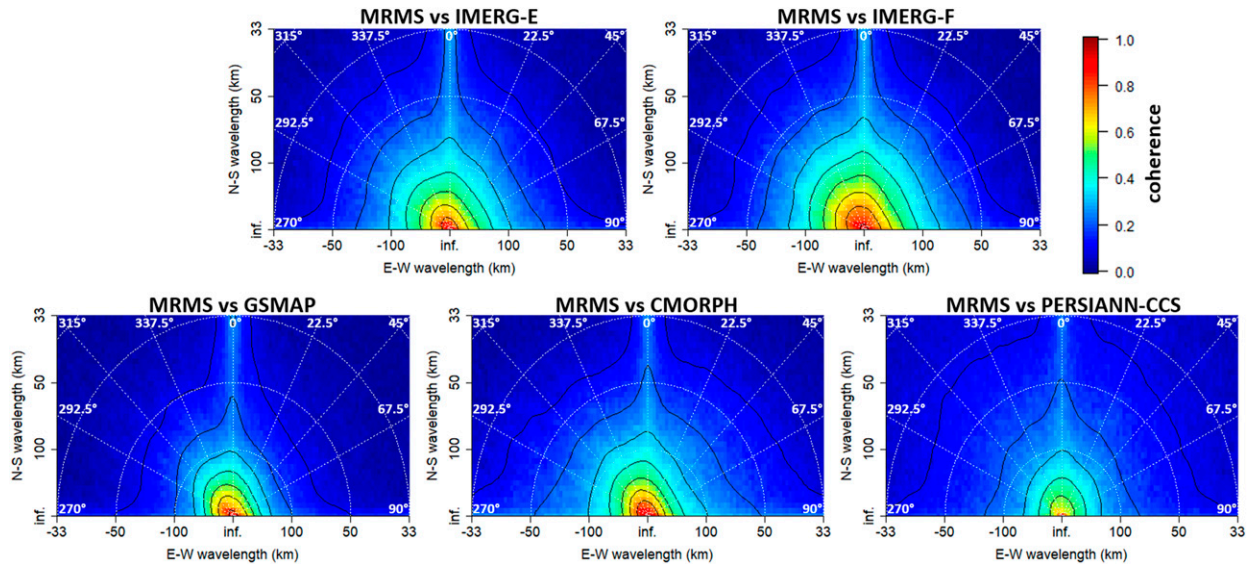


FIG. 7. Ability of the five satellite products to capture the location of precipitation features as functions of wavelength and azimuthal direction revealed by the spectral coherence with GV-MRMS over the southeastern United States. Spectral coherence (modulus) between the GV-MRMS and satellite precipitation fields as a function of the spatial wavenumbers in the east–west and north–south direction. The direction of the strongest gradients (northwest) is also the direction of the highest coherence for all products but PERSIANN-CCS. In all panels, smoothed isocontours are added at 0.1, 0.2, . . . , and 0.9 for enhanced visualization.

that, for the retrieval of precipitation from passive instruments in orbit, the “noise” is not only instrumental noise, but also variability in the measured radiances coming from physical phenomena concurrent with precipitation (e.g., variations in the surface temperature and emissivity).

### c. Joint space–time PSDs: Dynamics and propagative features

Moving into the assessment of precipitation space–time dynamics, the joint PSDs along the temporal dimension and first the east–west, then the north–south spatial directions are examined. Figure 9 shows the joint PSDs along the temporal dimension and the east–west spatial dimension. One immediately

notices the asymmetry, with most of the spectral power associated with negative wavenumbers, revealing the dominant eastward propagation of the precipitation features as already found for the case study in Fig. 3. For GV-MRMS, the spectral power is concentrated around the line corresponding to a  $\sim 60 \text{ km h}^{-1}$  velocity. For CMORPH and GSMaP the spectral energy is concentrated around the  $40\text{--}60 \text{ km h}^{-1}$  velocity, while for IMERG-E, IMERG-F, and PERSIANN-CCS the spectral power appears slightly shifted toward the higher velocities ( $60\text{--}90 \text{ km h}^{-1}$ ). From the space–time PSD, we compute the eastward over westward (E/W) power ratio as the ratio between the average spectral power for the negative and positive wavenumbers (Table 1). We exclude the wavenumbers

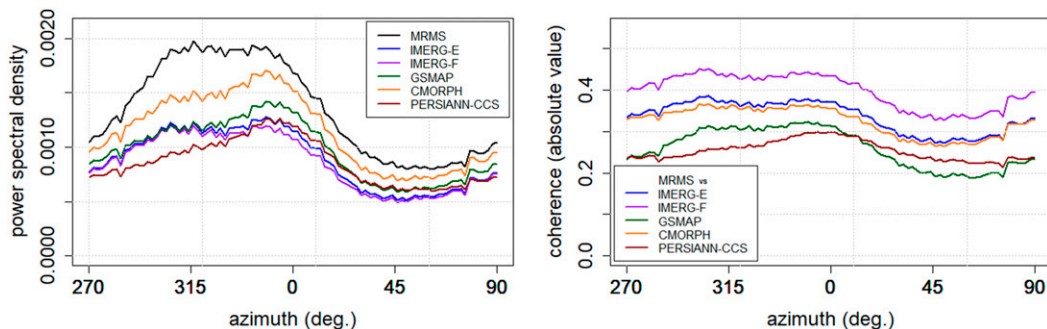


FIG. 8. Spatial variability of precipitation and consistency with GV-MRMS as a function of the azimuthal direction for the five satellite products. (left) PSDs of GV-MRMS and satellite precipitation fields averaged between wavelengths of 20 and 300 km as a function of the azimuthal direction. (right) Spectral coherence (modulus) between the GV-MRMS and satellite precipitation fields integrated between wavelengths of 20 and 300 km as a function of the azimuthal direction.

TABLE 1. Storm morphology and space–time dynamics spectral statistics for MRMS and the five satellite products over the southeastern United States for the 2018–20 period. The anisotropy factor is defined as the ratio of the maximum over the minimum of the PSD( $\theta$ ) function, where  $\theta$  is the azimuthal direction (see Fig. 8). The submeso power fraction is defined as the fraction of spectral power associated with wavelengths shorter than 300 km. The eastward over westward and northward over southward power ratios are derived from the joint space–time PSDs (Figs. 9 and S1) by integrating the PSDs over the negative and positive wavenumbers respectively (between the absolute wavelengths 20 and 500 km) and computing their ratio.

Product	Anisotropy factor	Submeso power fraction	E/W power ratio	N/S power ratio
MRMS	2.5	62%	2.5	1.5
IMERG-E	2.5	47%	2.7	1.1
IMERG-F	2.4	47%	2.9	1.0
GSMaP	2.4	51%	2.2	1.4
CMORPH	2.5	45%	3.1	1.2
PERSIANN-CCS	2.1	45%	1.5	1.2

longer than 500 km from the computation of the E/W power ratio because of the relatively poor spectral resolution at low wavenumbers. The E/W power ratio is a simple metric that compares the total energy of the eastward-propagating waves to the total energy of the westward-propagating waves. All products have an E/W power ratio higher than one, confirming the dominant eastward propagation. GV-MRMS has an E/W power ratio of 2.5, PERSIANN-CCS has an E/W power ratio of 1.5, and other satellite products have an E/W power ratio between 2.2 and 3.1. A possible partial explanation for these differences across the products in terms of propagation velocity and in terms of E/W power ratio is the difference in the way they integrate information from infrared cloud top temperature. The dynamics of cloud top temperature do not perfectly reflect the dynamics of precipitation. For example, the cloud top temperature is affected by atmospheric pressure waves which may propagate in a different direction and with a different phase velocity

than the motion of the clouds. These pressure waves may propagate upwind or downwind or be stationary; they are also generally dispersive (with a phase velocity changing with wavelength and frequency). Unlike the cloud top temperature, precipitation generally has a weak response to the short-length atmospheric waves. Among the other elements potentially affecting the space–time PSD of satellite products are nonpropagating artifacts generated by the microwave sampling scheme or the infrared cloud classification scheme for PERSIANN-CCS and IMERG.

From Fig. 10, one can see again that the frequencies and wavenumbers at which the spectral coherence between GV-MRMS and the satellite QPEs is the highest correspond to the frequencies and wavenumbers of maximal PSD. It is worth noting that the PSDs and coherences computed from 2 years of data provide results consistent with the case study presented in section 3, showing that this case study was in fact representative of

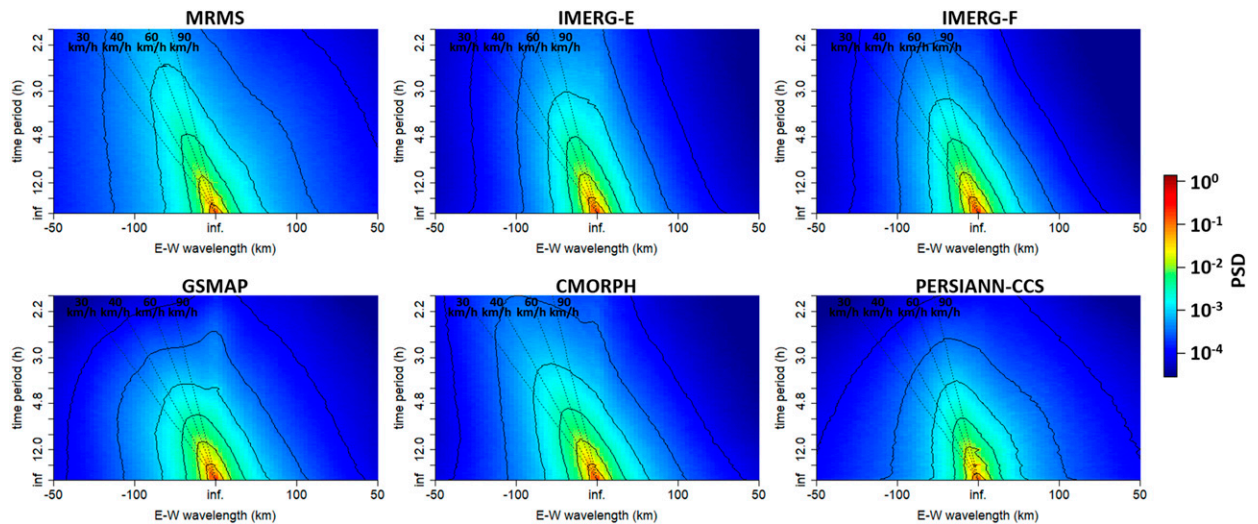


FIG. 9. Dynamics and longitudinal propagation of precipitation over the southeastern United States as revealed by the east–west space–time PSD. Joint spatiotemporal PSDs of the GV-MRMS and satellite precipitation fields in the east–west direction. Negative wavelengths correspond to eastward-propagating features and positive wavelengths to westward-propagating features. Most of the spectral power is associated with negative wavelengths (eastward propagation). The dotted lines correspond to nondispersive eastward propagation with velocity of 30, 40, 60, and 90 km h<sup>-1</sup>, from left to right, respectively. In all panels, smoothed isocontours are added at 10<sup>-0</sup>, 10<sup>-1</sup>, 10<sup>-2</sup>, 10<sup>-3</sup>, and 10<sup>-4</sup> for enhanced visualization.

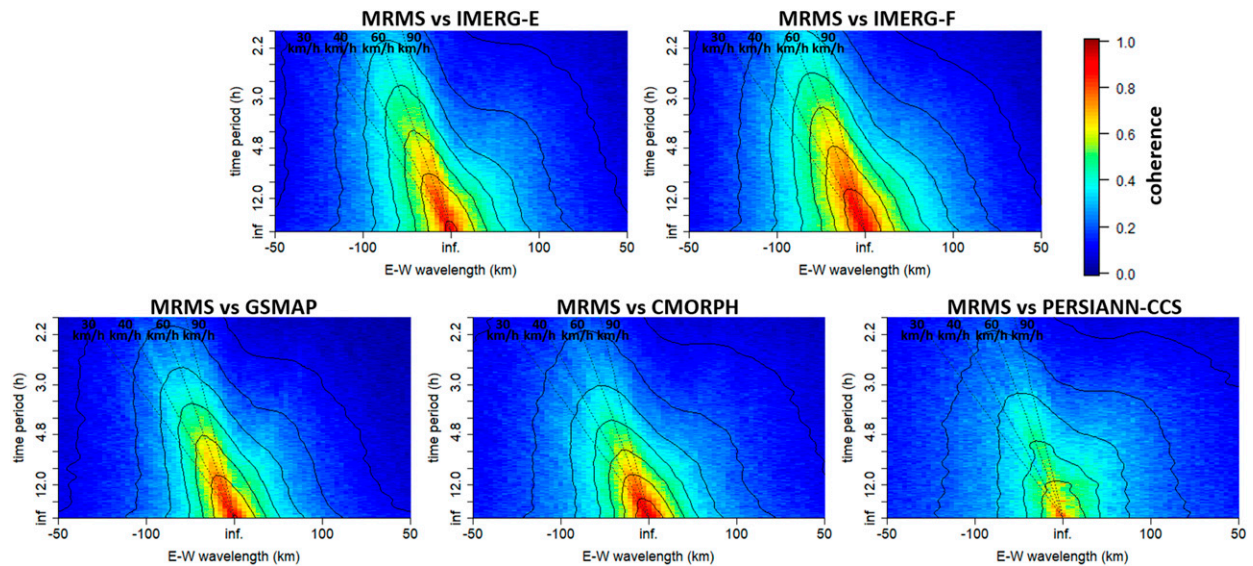


FIG. 10. Ability of the five satellite products to capture location and timing of longitudinal propagative precipitation features revealed by the spectral coherence with GV-MRMS over the southeastern United States. Spectral coherence (modulus) between the GV-MRMS and satellite precipitation fields as a function of the spatial wavenumber in the east–west direction and of the temporal frequency. The highest coherence corresponds to the dominant eastward propagating features. The dotted lines correspond to nondispersive eastward propagation with velocity of 30, 40, 60, and 90 km h<sup>-1</sup>, from left to right, respectively. In all panels, smoothed isocontours are added at 0.1, 0.2, . . . , and 0.9 for enhanced visualization.

the general topology and dynamics of the storm systems in the study area. The joint PSDs along the temporal dimension and the north–south spatial dimension are shown as Fig. S1 in the supplemental material. The asymmetry is not as pronounced as for the east–west direction, but one can still notice more power associated with northward-propagating features than with southward propagating features. The northward over southward (N/S) power ratio is found between 1 and 1.4 for the satellite products and 1.5 for GV-MRMS (Table 1). As for the east–west propagation (Fig. 10), the dominant propagating features for the north–south propagation are the ones for which the spectral coherence is the highest (Fig. S2). The argument of the spectral coherence (i.e., the phase shift) is not shown in the figures because it is not found to be significantly different from zero for any of the products at any wavenumber and any frequency. This indicates that the temporal delays or spatial shifts found between GV-MRMS and the satellite products are random, instead of being systematic.

Figure 11 (top) shows the omnidirectional space–time PSD of the GV-MRMS precipitation fields, obtained by performing circular integrals of the three-dimensional PSD in the  $k_x k_y$  plane (the omnidirectional spatial wavenumber being defined as  $k = \sqrt{k_x^2 + k_y^2}$ ). Other panels of Fig. 11 show the ratio of the satellite omnidirectional space–time PSDs over the omnidirectional space–time PSD of GV-MRMS. Independently of the temporal period, all the satellite products have a deficit of spectral power for wavelengths shorter than 100 or 200 km, consistent with what was shown by the spatial marginal PSD (Fig. 5). This deficit of spectral power is particularly pronounced at wavelengths shorter than 200 km and periods shorter than 4 h for GSMaP and PERSIANN-CCS. IMERG-E and IMERG-F

omnidirectional space–time PSDs appear highly similar down to the 6-h time period. IMERG-E shows an excess of spectral power relative to GV-MRMS at periods shorter than 6 h and wavelengths longer than 200 km. This indicates the IMERG-E shows excessively rapid changes in large-scale features. This unrealistic statistical property (large-scale features are normally expected to have a high temporal persistence) is likely to reflect retrieval artifacts. GSMaP, and to a lesser extent CMORPH and PERSIANN-CCS, also show this excess of spectral power at periods shorter than 6 h and wavelengths longer than 200 km. PERSIANN-CCS also shows an excess of spectral power at wavelengths shorter than 30 km, which reflects the existence of sharp transitions (“jumps”) in precipitation intensity between two adjacent pixels. This is likely an artifact coming from the PERSIANN-CCS cloud segmentation and classification scheme. This effect is also visible in a lesser degree in the IMERG products (which assimilate the PERSIANN-CCS estimates).

Figure 12 shows the spectral coherence of the satellite QPEs with GV-MRMS as a function of temporal period and omnidirectional spatial wavelength. For periods longer than 6 h the spectral coherence increases with increasing wavelength. At periods shorter than 6 h, the coherence is maximum for wavelengths between 150 and 300 km. Of all satellite products, IMERG-F appears to have the highest coherence with GV-MRMS at all wavelengths and periods. By setting a criterion of coherence with GV-MRMS higher than 0.7 ( $\approx \sqrt{1/2}$ , corresponding to 50% common variance and to a signal to noise ratio of 1:1 or 0 dB in log scale at the corresponding frequency and wavenumber), we assessed that the best performing multisatellite product, IMERG-F, resolves well the space–time dynamics of precipitation at spatial wavelengths down to

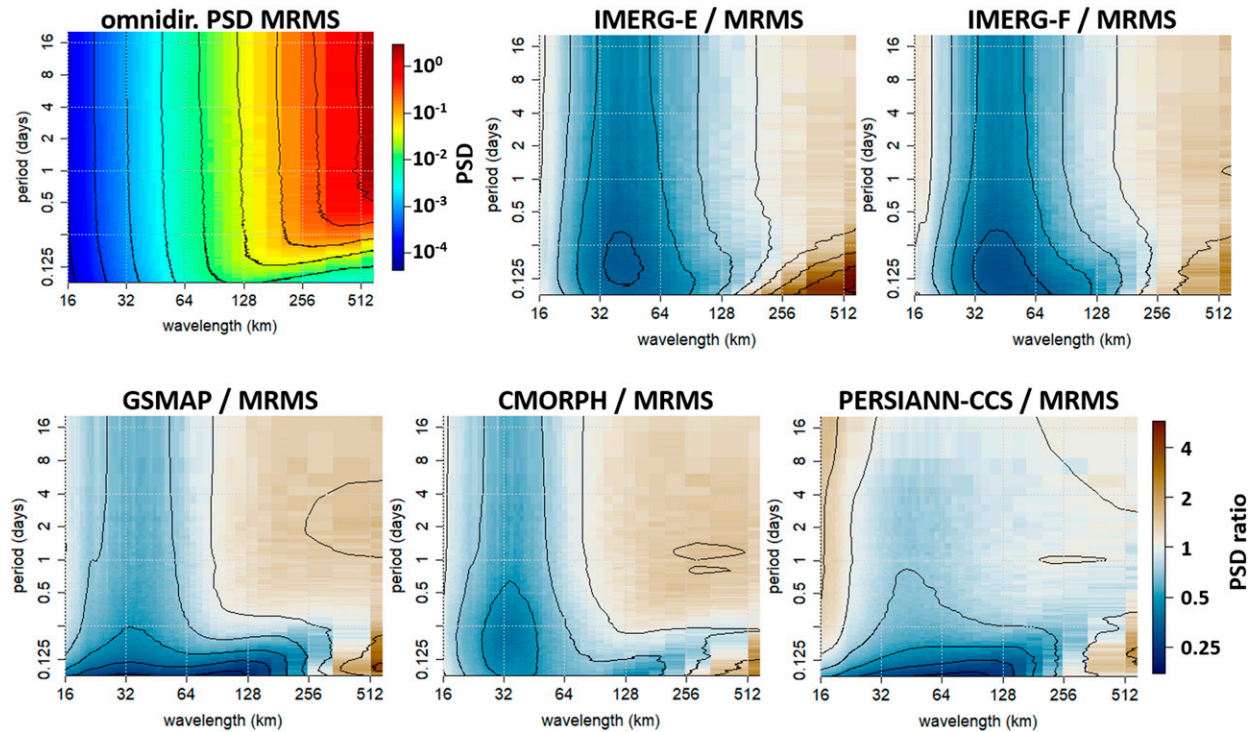


FIG. 11. Comparison of satellite products to GV-MRMS in terms of the distribution of spectral power across space–time scales. The top left panel shows the omnidirectional joint space–time PSD of GV-MRMS precipitation fields. The remaining panels show the ratio of the PSD of the satellite products over the PSD of GV-MRMS. Deficit of spectral power in satellite products at short wavelengths (shorter than 100 or 200 km) indicates spatially smooth retrieved precipitation fields, i.e., with high spatial correlation at short distances.

250 km and time periods down to 4 h, which corresponds to the transition between the mesoscale and the submesoscale. We note that, with the GPM constellation, for the study area and period, the average interval between two microwave observations is  $\sim 3$  h, which in theory allows one to resolve temporal periods down to  $\sim 6$  h at best (from the Nyquist–Shannon sampling theorem). The ability to resolve finer temporal periods must be attributed to the information provided by the motion vectors and the Geo-IR data.

We note that, for all satellite products, the spectral statistics (both the satellite over gauge–radar PSD ratio in Fig. 11 and the spectral coherence with GV-MRMS in Fig. 12) do not vary much with the time period within the range from 12 h to 20 days. This indicates that the spatial patterns of precipitation are not better retrieved at the 10 days aggregated time scale than at the 6 h aggregated time scale (while they are significantly better retrieved at the 6-h time scale than at the 1-h time scale).

### 5. Satellite spectral performances compared to a theoretical gauge network

An interesting question to ask is, “How many rain gauges is a satellite product worth?” i.e., what is the ability of the multisatellite products to capture the space–time dynamics of precipitation as compared to the ability of a gauge network? To provide insight into this question, we simulated the spatial sampling of a theoretical gauge network by subsampling the 1-km

half-hourly GV-MRMS precipitation fields and then interpolated the sparse samples. That is, we created fields of “virtual gauges” distributed on an isometric grid with desired gauge spacing. We used block kriging as the interpolation method with 10-km target resolution. We know a priori from the Nyquist–Shannon sampling theorem that a gauge spacing shorter than  $L/2$  is necessary to resolve the  $L$  wavelength. However, because the variability of precipitation at wavelengths shorter than  $L$  generates aliasing and sampling noise, this condition is generally not sufficient, and, depending on the rate of decrease of the PSD of precipitation with increasing wavelength, higher sampling rate may be necessary to achieve desired signal to noise ratio at wavelength  $L$ . We simulated several gauge networks and found that with an 80-km gauge spacing we obtain simulated retrieval performance similar to the actual performance of the satellite products.

The result of the spectral comparison of the interpolated virtual gauges with 80-km gauge spacing to the original GV-MRMS fields is shown on Fig. 13. Because kriging is a smooth interpolation, the interpolated fields show a deficit of spectral power at wavelengths shorter than 100 or 300 km, depending on the temporal period; the spectral coherence with GV-MRMS is also low at these scales. We notice an excess of spectral power at periods shorter than 6 h and wavelengths longer than 150 km in the interpolated precipitation compared to GV-MRMS. This additive signal at large spatial scales and high temporal frequencies corresponds to the sampling noise. The transition between the well-resolved periods and wavelengths (coherence

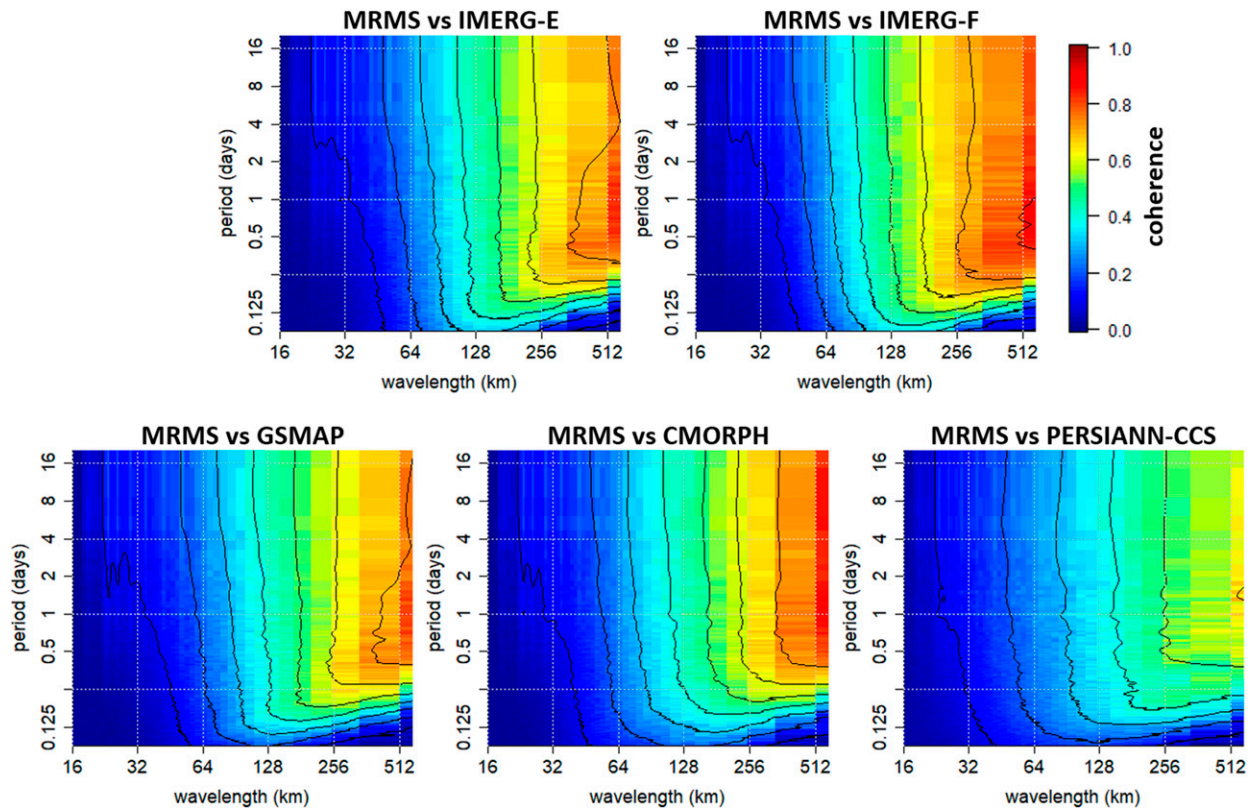


FIG. 12. Consistency between GV-MRMS and the satellite products in terms of the timing and location of the precipitation features as a function of the spatial wavelength and temporal period revealed by the omnidirectional spectral coherence. Spectral coherence (modulus) between the GV-MRMS and satellite precipitation fields as a function of the omnidirectional spatial wavelength and of the temporal period. For all products, the coherence is below 0.7 at wavelengths shorter than 250 km and periods shorter than 4 h. We consider these fine scales to be unresolved.

higher than 0.7) and the unresolved ones (coherence close to 0) is found to be sharper for the simulated gauge networks than for the satellite QPEs, presumably because of the regular spatial sampling of the simulated gauge network. In terms of spectral coherence with GV-MRMS, this idealized gauge network with 80-km gauge spacings show performance comparable with the best performing satellite QPE, IMERG-F. In other words, assuming that the results obtained here from 2 years of data over the southeastern United States are reasonable reflections of the products' global performances, over land, IMERG-F is equivalent to a global network of rain gauges spaced 80 km apart. We note that this simple setup only accounts for the effect of spatial sampling and ignores all other sources of error in gauge measurements, such as temporal sampling of tipping gauges, shot noise coming from the discrete occurrence of raindrops, wind effects, etc. (Habib et al. 2001; Kostinski et al. 2006; Kochendorfer et al. 2017). The subkilometer variability of precipitation is also ignored.

## 6. Discussion: Spectral bias, MSE reduction, and insights for retrieval algorithms

The results presented above show that all of the satellite QPEs evaluated have a deficit of spectral power at wavelengths

shorter than 200 km, revealing that they are spatially smooth precipitation estimates with excessive short-range spatial correlation. This “spectral bias” can be partially explained by the fact that the products rely on “smooth” mathematical operators designed to minimize the mean squared error (MSE) or to provide the most likely estimate given the observations. Among the smooth estimation methods are parametric regression and machine learning algorithms with quadratic cost functions, as well as Bayesian minimum MSE, maximum likelihood, or maximum a posteriori estimators. These types of methods generally produce spatially and temporally smooth estimates with reduced variance and reduction in extreme values (a simple manifestation of this phenomenon is for example the regression dilution in linear regression, (Spearman 1904). Of the satellite QPEs evaluated in the present article, the CMORPH, GSMaP, and IMERG algorithms implement a Kalman filter procedure, which is also a method prone to smoothing. The microwave radiative scheme used in the IMERG algorithm is a Bayesian minimum MSE algorithm (Randel et al. 2020). Smoothing effects also affect multisource merged estimates when the information provided by the different sources is not consistent. The kriging spatial interpolation method used in this article is also a minimum MSE method, hence the smoothness of the precipitation fields interpolated from the virtual gauges.

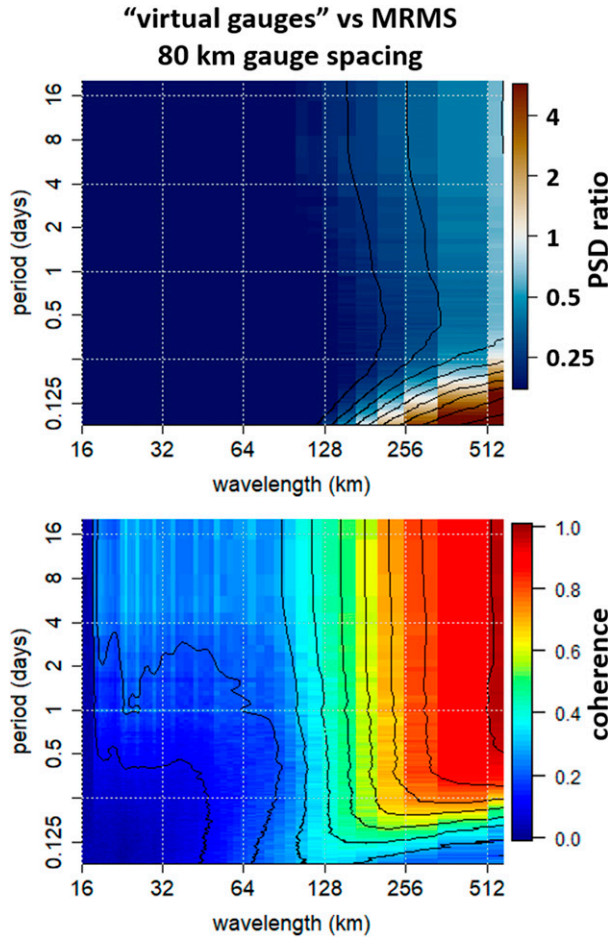


FIG. 13. Spectral performance of an idealized gauge network for comparison with the satellite products. (top) Ratio of the PSD of the interpolated “virtual rain gauges” network with 80-km gauge spacing over the PSD of GV-MRMS. (bottom) Spectral coherence (modulus) between the GV-MRMS and the interpolated virtual rain gauges as a function of the omnidirectional spatial wavelength and of the temporal period. By comparison with Fig. 12, it appears that IMERG-F shows spectral performance similar to this theoretical gauge network with 80-km gauge spacing.

The spectral unbiasing of the satellite products can be achieved by applying a multiplicative correction factor as a function of temporal frequency and spatial wavenumbers in the Fourier domain (to match the PSD of the radar fields). This unbiasing, as it is a linear filtering procedure, would not affect the spectral coherence between the satellite QPEs and the radar reference; however, it would affect the MSE, potentially increasing it, as discussed below. The spectral unbiasing of precipitation in global climate models has been proposed by Pierce et al. (2015), however only for the unidimensional temporal Fourier spectrum. One shall note that independently correcting the marginal spatial and temporal PSDs would not guarantee getting the right spatiotemporal PSD.

Histogram matching, also referred to in the literature as probability density function (PDF) matching, quantile matching,

or frequency matching, is a popular method for statistically correcting precipitation QPEs. It consists in applying a monotonic correction function to the precipitation rates to impose a PDF. This method allows one to compensate for the lack of variance and underrepresentation of extreme values in smooth QPEs. However, the histogram matching method only constrains the PDF at the “pixel” level; the effect of histogram matching on space–time correlation and PSD is a priori unknown. In contrast, constraining the space–time PSD allows one to constrain the second-order moment of the PDF (variance) at every spatiotemporal scale. More advanced spectral methods can constrain the multiscale higher-order moments (Harris et al. 2001).

Rather than performing the spectral unbiasing of the satellite QPEs to match the space–time PSD of the radar, one can perform optimal space–time filtering of the satellite QPEs to further minimize the mean squared difference with the radar (Turner et al. 2004; Guilloteau et al. 2018). The effect of the optimal filter is to suppress or reduce the variability in the satellite QPEs at the frequencies and wavenumbers at which the spectral coherence with the radar is low (and if necessary, at the frequencies and wavenumbers at which the PSD is overestimated by the satellites). As a linear filter, the optimal filter does not affect the spectral coherence with the radar. The PSD of the optimally filtered field is

$$P_{\text{opt}}(k_x, k_y, f) = |C(k_x, k_y, f)|^2 P_{\text{rad}}(k_x, k_y, f) \quad (7)$$

with  $C(k_x, k_y, f)$  the spectral coherence between the radar and the satellite QPE, and  $P_{\text{rad}}(k_x, k_y, f)$  the PSD of the radar field. One shall note that zero spectral bias, i.e.,  $P_{\text{sat}}(k_x, k_y, f) = P_{\text{rad}}(k_x, k_y, f)$ , and minimization of the MSE through space–time filtering cannot be achieved together when the coherence is different from 1. Indeed, when the coherence is lower than 1, the optimally filtered field is necessarily smoother (with lower PSD) than the radar reference. As already mentioned, the smoothness in QPEs is generally a side effect of quadratic or maximum likelihood optimization procedures. Therefore, spectral unbiasing and histogram matching generally have a deteriorating effect on the MSE and the correlation coefficient when comparing to a reference dataset, as they partially “undo” the work of the optimal operators. For example, with the satellite QPEs used in the present article, spectral unbiasing would amplify QPE’s variability at the high frequencies and wavenumbers, at which the spectral coherence with the radar is found to be low, and therefore lead to higher mean squared difference with the radar. This can be related to the concept of “double penalty,” which is that, in terms of MSE or correlation with a reference dataset, it is more unfavorable to retrieve a feature with the wrong timing/location than to not retrieve the feature at all (Rossa et al. 2008).

This raises an important question for precipitation estimation: when is minimizing the MSE more important than preserving the statistical properties of precipitation fields (in particular the PDF of precipitation rates and the space–time PSD or autocorrelation), and vice versa? A more technical formulation of this question is: what cost function should be minimized by optimization procedures and machine-learning algorithms for precipitation estimation (Ning et al. 2014;

Ebtehaj et al. 2014, 2015; Wang et al. 2020; Li et al. 2021)? Obviously, the answer mostly depends on the application. However, because MSE and correlation with a reference product are the most commonly used metrics when QPEs are validated and evaluated, product makers may be inclined to favor these over other aspects. Additionally, the reference datasets against which the products are evaluated may themselves also rely on smooth quadratic or maximum likelihood operators (e.g., kriging or other smooth interpolation methods). In that case, similarly smooth precipitation estimates show more favorable statistics when compared to these references. Indeed, the frequency/wavelength dependent biases and the intensity dependent biases (conditional biases, Ciach et al. 2000; Kirstetter et al. 2013) introduced by the optimization procedures in the retrieval algorithms can cause estimates derived from totally independent sources to have mutually correlated errors. A potential solution to achieve simultaneously both objectives of preserving the true PSD of precipitation and minimizing the MSE is to embrace the satellite QPEs' uncertainty through a multiscale probabilistic/ensemble approach, where each individual realization of the ensemble has a realistic space–time PSD and the ensemble mean constitutes the minimal MSE estimate (Bellerby and Sun 2005; Guilloteau et al. 2018). This approach, which consists in generating ensembles constrained by the observations with an underlying stochastic precipitation model, has also been proposed to derive precipitation fields from gauge and radar measurements (Haberlandt and Gattke 2004; Vischel et al. 2009; AghaKouchak et al. 2010).

## 7. Concluding remarks

The space–time Fourier spectral analysis of five satellite QPEs and of the GV-MRMS gauge–radar product over the southeastern United States reveals high consistency between the GV-MRMS gauge–radar product and the GSMaP, CMORPH, and IMERG multisatellite products, which all rely partially on microwave satellite measurements, down to the 250-km spatial wavelength and the 4-h temporal period. At these relatively coarse scales, the consistency between the PSDs of the satellite and gauge–radar fields indicates statistically similar spatio-temporal dynamics; additionally, the high spectral coherence ( $>0.7$ ) between the satellite products and GV-MRMS indicates agreement in terms of location and timing of the precipitation features. IMERG-F is the product showing the highest spectral coherence with GV-MRMS at all frequencies and wavenumbers. At shorter periods and wavelengths, all satellite products show a deficit of spectral power (i.e., excessive smoothness) and a low spectral coherence with GV-MRMS. However, consistent patterns in the joint space–time PSDs reveals that they properly characterize the average spatial anisotropy and the dominant propagative features in terms of speed and direction at all scales for the area and period of the study.

Concerning the Early and Final versions of the IMERG product, the differences between the two lie essentially in a higher level of noise at large spatial wavelengths and high temporal frequency in IMERG-E. We note that in terms of spectral characteristics, this noise is somewhat similar to the

sampling noise in spatially interpolated precipitation from point measurements. In the end, we find that the better performance of IMERG-F compared to the other products lies essentially in a better ability to resolve spatial wavelengths greater than 200 km. Resolving the submesoscale dynamics of precipitation from passive satellite instruments and the existing constellation of satellites remains an ongoing challenge.

The performance metrics given in the present article are bulk statistics computed from more than 2 years of data and over more than 2 million km<sup>2</sup> area in the southeastern United States. In general, the retrieval performances of satellite products are expected to vary with time and location. For example, retrieval performances are known to be dependent on the type of precipitation system (such as convective and stratiform precipitation). However, the multiscale nature of the present analysis does not allow us to separate precipitation types, since, at any scale, every observed scene contains a mixture of different precipitation types. Another factor of performance variability for satellite products relying on several low-orbit instruments is the instantaneous configuration of the constellation. Indeed, the scenes directly sampled by one or several microwave imagers are likely better resolved than the scenes for which the estimates rely on dynamical interpolation and motion vectors. Recent studies (Tan et al. 2021; Rajagopal et al. 2021) have identified in IMERG data a dependence of the precipitation statistics on the delay between the retrieval time and the actual time of the closest microwave observation at given point. One should note that the orbits of the different microwave radiometers of the constellation on which the CMORPH, GSMaP, and IMERG products rely are not synchronized, and therefore the temporal sampling at a given point is irregular. The Kalman filters in CMORPH, GSMaP, and IMERG are expected to cause more pronounced space–time smoothing when few microwave observations are available within a given time frame. Ongoing developments for future versions of the IMERG algorithm include the SHARPEN method (Scheme for Histogram Adjustment with Ranked Precipitation Estimates in the Neighborhood; Tan et al. 2021), designed to compensate for the statistical smoothing resulting from the Kalman filtering through a local histogram matching approach.

The elements mentioned in the discussion about the spectral bias, which reflects the statistical smoothness of precipitation estimates, and its relation to the algorithmic optimization procedures (section 6) are valid for any retrieved spatiotemporal variable. However, the relatively large uncertainties that exist in the measurement and prediction of precipitation at the submesoscale, and the importance of precipitation extreme statistics in hydrology, climate science and risk management make them particularly relevant in the case of precipitation. Space–time filtering as postprocessing to enhance fine-scale variability is a potential solution to correct for the smoothness of satellite precipitation products.

*Acknowledgments.* This research was supported by NASA through the Global Precipitation Measurement program (Grants 80NSSC19K0684, 80NSSC19K068 and WBS-573945.04.80.01.01) and the Ground Validation Program (Grant NNX16AL23G). The National Science Foundation (NSF) supported this research

under the EAGER program (Grant ECCS-1839441) and the TRIPODS+X program (GrantDMS-1839336). Additionally, the support by NASA (Grant 80NSSC19K0726) and NSF (Grant EAR-1928724) for the organization of the 12th International Precipitation Conference (IPC12) and production of the IPC12 AMS special collection of papers is gratefully acknowledged.

*Data availability statement.* Part of the GV-MRMS data used in this study is available at <http://dx.doi.org/10.5067/GPM/GV/MRMS/DATA101>. The satellite products are publicly available: CMOPRH at <https://doi.org/10.25921/w9va-q159>; GSMAP at <https://sharaku.eorc.jaxa.jp/GSMaP>; PERSIANN-CCS at <https://chrsdata.eng.uci.edu>; IMERG-E at <https://doi.org/10.5067/GPM/IMERG/3B-HH-E/06>; and IMERG-F at <https://doi.org/10.5067/GPM/IMERG/3B-HH/06>.

#### REFERENCES

- AghaKouchak, A., A. Bárdossy, and E. Habib, 2010: Conditional simulation of remotely sensed rainfall data using a non-Gaussian  $v$ -transformed copula. *Adv. Water Resour.*, **33**, 624–634, <https://doi.org/10.1016/j.advwatres.2010.02.010>.
- Ayat, H., J. P. Evans, S. Sherwood, and A. Behrangi, 2021: Are storm characteristics the same when viewed using merged surface radars or a merged satellite product? *J. Hydrometeorol.*, **22**, 43–62, <https://doi.org/10.1175/JHM-D-20-0187.1>.
- Beck, H. E., and Coauthors, 2019: Daily evaluation of 26 precipitation datasets using Stage-IV gauge-radar data for the CONUS. *Hydrol. Earth Syst. Sci.*, **23**, 207–224, <https://doi.org/10.5194/hess-23-207-2019>.
- Bellerby, T. J., and J. Sun, 2005: Probabilistic and ensemble representations of the uncertainty in an IR/microwave satellite precipitation product. *J. Hydrometeorol.*, **6**, 1032–1044, <https://doi.org/10.1175/JHM454.1>.
- Casse, C., and M. Gosset, 2015: Analysis of hydrological changes and flood increase in Niamey based on the PERSIANN-CDR satellite rainfall estimate and hydrological simulations over the 1983–2013 period. *Proc. IAHS*, **370**, 117–123, <https://doi.org/10.5194/piahs-370-117-2015>.
- Céron, J. P., and J. F. Guérémy, 1999: Validation of the space–time variability of African easterly waves simulated by the CNRM GCM. *J. Climate*, **12**, 2831–2855, [https://doi.org/10.1175/1520-0442\(1999\)012<2831:VOTSTV>2.0.CO;2](https://doi.org/10.1175/1520-0442(1999)012<2831:VOTSTV>2.0.CO;2).
- Ciach, G. J., M. L. Morrissey, and W. F. Krajewski, 2000: Conditional bias in radar rainfall estimation. *J. Appl. Meteor. Climatol.*, **39**, 1941–1946, [https://doi.org/10.1175/1520-0450\(2000\)039<1941:CBIRRE>2.0.CO;2](https://doi.org/10.1175/1520-0450(2000)039<1941:CBIRRE>2.0.CO;2).
- Cohen, L., 1998: The generalization of the Wiener-Khinchin theorem. *Proc. 1998 IEEE Int. Conf. on Acoustics, Speech and Signal Processing*, Seattle, WA, Institute of Electrical and Electronics Engineers, 1577–1580, <https://doi.org/10.1109/ICASSP.1998.681753>.
- Dai, A., X. Lin, and K. L. Hsu, 2007: The frequency, intensity, and diurnal cycle of precipitation in surface and satellite observations over low- and mid-latitudes. *Climate Dyn.*, **29**, 727–744, <https://doi.org/10.1007/s00382-007-0260-y>.
- Demaria, E. M. C., D. A. Rodriguez, E. E. Ebert, P. Salio, F. Su, and J. B. Valdes, 2011: Evaluation of mesoscale convective systems in South America using multiple satellite products and an object-based approach. *J. Geophys. Res.*, **116**, D08103, <https://doi.org/10.1029/2010JD015157>.
- De Michele, C., and P. Bernardara, 2005: Spectral analysis and modeling of space-time rainfall fields. *Atmos. Res.*, **77**, 124–136, <https://doi.org/10.1016/j.atmosres.2004.10.031>.
- Derin, Y., and Coauthors, 2016: Multiregional satellite precipitation products evaluation over complex terrain. *J. Hydrometeorol.*, **17**, 1817–1836, <https://doi.org/10.1175/JHM-D-15-0197.1>.
- Ebert, E. E., and J. L. McBride, 2000: Verification of precipitation in weather systems: Determination of systematic errors. *J. Hydrol.*, **239**, 179–202, [https://doi.org/10.1016/S0022-1694\(00\)00343-7](https://doi.org/10.1016/S0022-1694(00)00343-7).
- Ebtehaj, A. M., M. Zupanski, G. Lerman, and E. Foufoula-Georgiou, 2014: Variational data assimilation via sparse regularisation. *Tellus*, **66A**, 21789, <https://doi.org/10.3402/tellusa.v66.21789>.
- , R. L. Bras, and E. Foufoula-Georgiou, 2015: Shrunk locally linear embedding for passive microwave retrieval of precipitation. *IEEE Trans. Geosci. Remote Sens.*, **53**, 3720–3736, <https://doi.org/10.1109/TGRS.2014.2382436>.
- Ghil, M., and Coauthors, 2002: Advanced spectral methods for climatic time series. *Rev. Geophys.*, **40**, 1003, <https://doi.org/10.1029/2000RG000092>.
- Gilman, D. L., F. J. Fuglister, and J. M. Mitchell Jr., 1963: On the power spectrum of “red noise.” *J. Atmos. Sci.*, **20**, 182–184, [https://doi.org/10.1175/1520-0469\(1963\)020<0182:OTPSO>2.0.CO;2](https://doi.org/10.1175/1520-0469(1963)020<0182:OTPSO>2.0.CO;2).
- Guiloteau, C., and E. Foufoula-Georgiou, 2020: Multiscale evaluation of satellite precipitation products: Effective resolution of IMERG. *Satellite Precipitation Measurement*, V. Levizzani et al., Ed., Springer, 533–558, [https://doi.org/10.1007/978-3-030-35798-6\\_5](https://doi.org/10.1007/978-3-030-35798-6_5).
- , M. Gosset, C. Vignolles, M. Alcoba, Y. M. Tourre, and J. P. Lacaux, 2014: Impacts of satellite-based rainfall products on predicting spatial patterns of Rift Valley fever vectors. *J. Hydrometeorol.*, **15**, 1624–1635, <https://doi.org/10.1175/JHM-D-13-0134.1>.
- , E. Foufoula-Georgiou, and C. D. Kummerow, 2017: Global multiscale evaluation of satellite passive microwave retrieval of precipitation during the TRMM and GPM eras: Effective resolution and regional diagnostics for future algorithm development. *J. Hydrometeorol.*, **18**, 3051–3070, <https://doi.org/10.1175/JHM-D-17-0087.1>.
- , R. Roca, M. Gosset, and V. Venugopal, 2018: Stochastic generation of precipitation fraction at high resolution with a multiscale constraint from satellite observations. *Quart. J. Roy. Meteor. Soc.*, **144**, 176–190, <https://doi.org/10.1002/qj.3314>.
- Haberlandt, U., and C. Gattke, 2004: Spatial interpolation vs. simulation of precipitation for rainfall-runoff modelling—A case study in the Lippe River basin. *Hydrology: Science and practice for the 21st century: Proceedings of the British Hydrological Society International Conference*, B. Webb et al., Eds., British Hydrological Society, 120–127.
- Habib, E., W. F. Krajewski, and A. Kruger, 2001: Sampling errors of tipping-bucket rain gauge measurements. *J. Hydrol. Eng.*, **6**, 159–166, [https://doi.org/10.1061/\(ASCE\)1084-0699\(2001\)6:2\(159\)](https://doi.org/10.1061/(ASCE)1084-0699(2001)6:2(159)).
- Harris, D., E. Foufoula-Georgiou, K. K. Droegemeier, and J. J. Levit, 2001: Multiscale statistical properties of a high-resolution precipitation forecast. *J. Hydrometeorol.*, **2**, 406–418, [https://doi.org/10.1175/1525-7541\(2001\)002<0406:MSPOAH>2.0.CO;2](https://doi.org/10.1175/1525-7541(2001)002<0406:MSPOAH>2.0.CO;2).
- Hayashi, Y., 1982: Space-time spectral analysis and its applications to atmospheric waves. *J. Meteor. Soc. Japan*, **60**, 156–171, [https://doi.org/10.2151/jmsj1965.60.1\\_156](https://doi.org/10.2151/jmsj1965.60.1_156).
- Hilker, T., and Coauthors, 2014: Vegetation dynamics and rainfall sensitivity of the Amazon. *Proc. Natl. Acad. Sci. USA*, **111**, 16 041–16 046, <https://doi.org/10.1073/pnas.1404870111>.
- Hong, Y., K. L. Hsu, S. Sorooshian, and X. Gao, 2004: Precipitation estimation from remotely sensed imagery using an artificial neural network cloud classification system. *J. Appl. Meteor.*, **43**, 1834–1853, <https://doi.org/10.1175/JAM2173.1>.

- Hou, A. Y., and Coauthors, 2014: The Global Precipitation Measurement mission. *Bull. Amer. Meteor. Soc.*, **95**, 701–722, <https://doi.org/10.1175/BAMS-D-13-00164.1>.
- Huffman, G. J., and Coauthors, 2019: NASA Global Precipitation Measurement (GPM) Integrated Multi-satellite Retrievals for GPM (IMERG). Algorithm Theoretical Basis Doc., version 06, 34 pp., [https://gpm.nasa.gov/sites/default/files/2019-05/IMERG\\_ATBD\\_V06.pdf](https://gpm.nasa.gov/sites/default/files/2019-05/IMERG_ATBD_V06.pdf).
- Joyce, R. J., and P. Xie, 2011: Kalman filter-based CMORPH. *J. Hydrometeorol.*, **12**, 1547–1563, <https://doi.org/10.1175/JHM-D-11-022.1>.
- , J. E. Janowiak, P. A. Arkin, and P. Xie, 2004: CMORPH: A method that produces global precipitation estimates from passive microwave and infrared data at high spatial and temporal resolution. *J. Hydrometeorol.*, **5**, 487–503, [https://doi.org/10.1175/1525-7541\(2004\)005<0487:CAMTPG>2.0.CO;2](https://doi.org/10.1175/1525-7541(2004)005<0487:CAMTPG>2.0.CO;2).
- Kao, S. K., and L. L. Wendell, 1970: The kinetic energy of the large-scale atmospheric motion in wavenumber-frequency space: I. Northern Hemisphere. *J. Atmos. Sci.*, **27**, 359–375, [https://doi.org/10.1175/1520-0469\(1970\)027<0359:TKEOTL>2.0.CO;2](https://doi.org/10.1175/1520-0469(1970)027<0359:TKEOTL>2.0.CO;2).
- Kerns, B. W., and S. S. Chen, 2020: A 20-year climatology of Madden-Julian Oscillation convection: Large-scale precipitation tracking from TRMM-GPM rainfall. *J. Geophys. Res.*, **125**, e2019JD032142, <https://doi.org/10.1029/2019JD032142>.
- Kirschbaum, D. B., and T. Stanley, 2018: Satellite-based assessment of rainfall-triggered landslide hazard for situational awareness. *Earth's Future*, **6**, 505–523, <https://doi.org/10.1002/2017EF000715>.
- , and Coauthors, 2017: NASA's remotely sensed precipitation: A reservoir for applications users. *Bull. Amer. Meteor. Soc.*, **98**, 1169–1184, <https://doi.org/10.1175/BAMS-D-15-00296.1>.
- Kirstetter, P.-E., and Coauthors, 2012: Toward a framework for systematic error modeling of spaceborne precipitation radar with NOAA/NSSL ground radar-based national mosaic QPE. *J. Hydrometeorol.*, **13**, 1285–1300, <https://doi.org/10.1175/JHM-D-11-0139.1>.
- , N. Viltard, and M. Gosset, 2013: An error model for instantaneous satellite rainfall estimates: Evaluation of BRAIN-TMI over West Africa. *Quart. J. Roy. Meteor. Soc.*, **139**, 894–911, <https://doi.org/10.1002/qj.1964>.
- , W. A. Petersen, C. D. Kummerow, and D. B. Wolff, 2020: Integrated multi-satellite evaluation for the Global Precipitation Measurement mission: Impact of precipitation types on spaceborne precipitation estimation. *Satellite Precipitation Measurement*, V. Levizzani et al., Eds., Springer, 583–608, [https://doi.org/10.1007/978-3-030-35798-6\\_7](https://doi.org/10.1007/978-3-030-35798-6_7).
- Kochendorfer, J., and Coauthors, 2017: The quantification and correction of wind-induced precipitation measurement errors. *Hydrol. Earth Syst. Sci.*, **21**, 1973–1989, <https://doi.org/10.5194/hess-21-1973-2017>.
- Kostinski, A. B., M. L. Larsen, and A. R. Jameson, 2006: The texture of rain: Exploring stochastic micro-structure at small scales. *J. Hydrol.*, **328**, 38–45, <https://doi.org/10.1016/j.jhydrol.2005.11.035>.
- Kummerow, C., and Coauthors, 2000: The status of the Tropical Rainfall Measuring Mission (TRMM) after two years in orbit. *J. Appl. Meteor.*, **39**, 1965–1982, [https://doi.org/10.1175/1520-0450\(2001\)040<1965:TSOTTR>2.0.CO;2](https://doi.org/10.1175/1520-0450(2001)040<1965:TSOTTR>2.0.CO;2).
- Kundu, P. K., and T. L. Bell, 2003: A stochastic model of space-time variability of mesoscale rainfall: Statistics of spatial averages. *Water Resour. Res.*, **39**, 1328, <https://doi.org/10.1029/2002WR001802>.
- Kyriakidis, P. C., and A. G. Journel, 1999: Geostatistical space-time models: A review. *Math. Geol.*, **31**, 651–684, <https://doi.org/10.1023/A:1007528426688>.
- Li, Z., D. B. Wright, S. Q. Zhang, D. B. Kirschbaum, and S. H. Hartke, 2020: Object-based comparison of data-driven and physics-driven satellite estimates of extreme rainfall. *J. Hydrometeorol.*, **21**, 2759–2776, <https://doi.org/10.1175/JHM-D-20-0041.1>.
- Li, Z., Y. Wen, M. Schreier, A. Behrangi, Y. Hong, and B. Lambriksen, 2021: Advancing satellite precipitation retrievals with data driven approaches: Is black box model explainable? *Earth Space Sci.*, **8**, e2020EA001423, <https://doi.org/10.1029/2020EA001423>.
- Lin, J. L., and Coauthors, 2006: Tropical intraseasonal variability in 14 IPCC AR4 climate models. Part I: Convective signals. *J. Climate*, **19**, 2665–2690, <https://doi.org/10.1175/JCLI3735.1>.
- Lovejoy, S., and D. Schertzer, 1986: Scale invariance, symmetries, fractals, and stochastic simulations of atmospheric phenomena. *Bull. Amer. Meteor. Soc.*, **67**, 21–32, [https://doi.org/10.1175/1520-0477\(1986\)067<0021:SISFAS>2.0.CO;2](https://doi.org/10.1175/1520-0477(1986)067<0021:SISFAS>2.0.CO;2).
- Mehta, A. V., and S. Yang, 2008: Precipitation climatology over Mediterranean Basin from ten years of TRMM measurements. *Adv. Geosci.*, **17**, 87–91, <https://doi.org/10.5194/adgeo-17-87-2008>.
- Newton, C. W., 1950: Structure and mechanism of the prefrontal squall line. *J. Atmos. Sci.*, **7**, 210–222, [https://doi.org/10.1175/1520-0469\(1950\)007<0210:SAMOTZ>2.0.CO;2](https://doi.org/10.1175/1520-0469(1950)007<0210:SAMOTZ>2.0.CO;2).
- Nguyen, P., and Coauthors, 2020: PERSIANN Dynamic Infrared-Rain Rate (PDIR-Now): A near-real-time, quasi-global satellite precipitation dataset. *J. Hydrometeorol.*, **21**, 2893–2906, <https://doi.org/10.1175/JHM-D-20-0177.1>.
- Ning, L., F. P. Carli, A. M. Ebtehaj, E. Foufoula-Georgiou, and T. T. Georgiou, 2014: Coping with model error in variational data assimilation using optimal mass transport. *Water Resour. Res.*, **50**, 5817–5830, <https://doi.org/10.1002/2013WR014966>.
- Orbe, C., and Coauthors, 2020: Representation of modes of variability in six US climate models. *J. Climate*, **33**, 7591–7617, <https://doi.org/10.1175/JCLI-D-19-0956.1>.
- Oreopoulos, L., A. Marshak, R. F. Cahalan, and G. Wen, 2000: Cloud three-dimensional effects evidenced in Landsat spatial power spectra and autocorrelation functions. *J. Geophys. Res.*, **105**, 14 777–14 788, <https://doi.org/10.1029/2000JD900153>.
- Petersen, W. A., P. E. Kirstetter, J. Wang, D. B. Wolff, and A. Tokay, 2020: The GPM ground validation program. *Satellite Precipitation Measurement*, V. Levizzani et al., Eds., Springer, 471–502, [https://doi.org/10.1007/978-3-030-35798-6\\_2](https://doi.org/10.1007/978-3-030-35798-6_2).
- Pierce, D. W., D. R. Cayan, E. P. Maurer, J. T. Abatzoglou, and K. C. Hegewisch, 2015: Improved bias correction techniques for hydrological simulations of climate change. *J. Hydrometeorol.*, **16**, 2421–2442, <https://doi.org/10.1175/JHM-D-14-0236.1>.
- Proakis, J. G., and D. G. Manolakis, 2001: Nonparametric methods for power spectrum estimation. *Digital Signal Processing: Principles, Algorithms and Applications*, 3rd ed. Prentice-Hall, 908–919.
- Rajagopal, M., E. Zipser, G. Huffman, J. Russell, and J. Tan, 2021: Comparisons of IMERG version 06 precipitation at and between passive microwave overpasses in the tropics. *J. Hydrometeorol.*, **22**, 2117–2130, <https://doi.org/10.1175/JHM-D-20-0226.1>.
- Randel, D. L., C. D. Kummerow, and S. Ringerud, 2020: The Goddard Profiling (GPROF) precipitation retrieval algorithm. *Satellite Precipitation Measurement*, V. Levizzani et al., Eds., Springer, 141–152, [https://doi.org/10.1007/978-3-030-24568-9\\_8](https://doi.org/10.1007/978-3-030-24568-9_8).
- Roca, R., J. Aublanc, P. Chambon, T. Fiolleau, and N. Viltard, 2014: Robust observational quantification of the contribution of mesoscale convective systems to rainfall in the tropics. *J. Climate*, **27**, 4952–4958, <https://doi.org/10.1175/JCLI-D-13-00628.1>.

- Rossa, A., P. Nurmi, and E. Ebert, 2008: Overview of methods for the verification of quantitative precipitation forecasts. *Precipitation: Advances in Measurement, Estimation and Prediction*, S. Michaelides, Ed., Springer, 419–452.
- Rysman, J. F., S. Verrier, Y. Lemaître, and E. Moreau, 2013: Space-time variability of the rainfall over the western Mediterranean region: A statistical analysis. *J. Geophys. Res. Atmos.*, **118**, 8448–8459, <https://doi.org/10.1002/jgrd.50656>.
- Spapiano, M. R. P., and P. A. Arkin, 2009: An intercomparison and validation of high-resolution satellite precipitation estimates with 3-hourly gauge data. *J. Hydrometeorol.*, **10**, 149–166, <https://doi.org/10.1175/2008JHM1052.1>.
- Spearman, C., 1904: The proof and measurement of association between two things. *Amer. J. Psychol.*, **15**, 72–101, <https://doi.org/10.2307/1412159>.
- Suepa, T., J. Qi, S. Lawawirojwong, and J. P. Messina, 2016: Understanding spatio-temporal variation of vegetation phenology and rainfall seasonality in the monsoon Southeast Asia. *Environ. Res.*, **147**, 621–629, <https://doi.org/10.1016/j.envres.2016.02.005>.
- Tan, J., G. J. Huffman, D. T. Bolvin, and E. J. Nelkin, 2019: IMERG V06: Changes to the morphing algorithm. *J. Atmos. Oceanic Technol.*, **36**, 2471–2482, <https://doi.org/10.1175/JTECH-D-19-0114.1>.
- , —, —, —, and M. Rajagopal, 2021: SHARPEN: A scheme to restore the distribution of averaged precipitation fields. *J. Hydrometeorol.*, **22**, 2105–2116, <https://doi.org/10.1175/JHM-D-20-0225.1>.
- Tapiador, F. J., C. Marcos, and J. M. Sancho, 2019: The convective rainfall rate from cloud physical properties algorithm for Meteosat second-generation satellites: Microphysical basis and intercomparisons using an object-based method. *Remote Sens.*, **11**, 527, <https://doi.org/10.3390/rs11050527>.
- Turner, B. J., I. Zawadzki, and U. Germann, 2004: Predictability of precipitation from continental radar images. Part III: Operational nowcasting implementation (MAPLE). *J. Appl. Meteor. Climatol.*, **43**, 231–248, [https://doi.org/10.1175/1520-0450\(2004\)043<0231:POPFCR>2.0.CO;2](https://doi.org/10.1175/1520-0450(2004)043<0231:POPFCR>2.0.CO;2).
- Tustison, B., D. Harris, and E. Foufoula-Georgiou, 2001: Scale issues in verification of precipitation forecasts. *J. Geophys. Res.*, **106**, 11 775–11 784, <https://doi.org/10.1029/2001JD900066>.
- Ushio, T., and Coauthors, 2009: A Kalman filter approach to the Global Satellite Mapping of Precipitation (GSMaP) from combined passive microwave and infrared radiometric data. *J. Meteor. Soc. Japan*, **87A**, 137–151, <https://doi.org/10.2151/jmsj.87A.137>.
- Vischel, T., T. Lebel, S. Massuel, and B. Cappelaere, 2009: Conditional simulation schemes of rain fields and their application to rainfall-runoff modeling studies in the Sahel. *J. Hydrol.*, **375**, 273–286, <https://doi.org/10.1016/j.jhydrol.2009.02.028>.
- Wang, G., W. Han, and S. Lu, 2020: Precipitation retrieval by the L1-norm regularization: Typhoon Hagibis case. *Quart. J. Roy. Meteor. Soc.*, **147**, 773–785, <https://doi.org/10.1002/qj.3945>.
- Waymire, E. D., and V. K. Gupta, 1981: The mathematical structure of rainfall representations: 1. A review of the stochastic rainfall models. *Water Resour. Res.*, **17**, 1261–1272, <https://doi.org/10.1029/WR017i005p01261>.
- Wheeler, M., and G. N. Kiladis, 1999: Convectively coupled equatorial waves: Analysis of clouds and temperature in the wavenumber-frequency domain. *J. Atmos. Sci.*, **56**, 374–399, [https://doi.org/10.1175/1520-0469\(1999\)056<0374:CCEWAO>2.0.CO;2](https://doi.org/10.1175/1520-0469(1999)056<0374:CCEWAO>2.0.CO;2).
- Xie, P., R. Joyce, S. Wu, S. H. Yoo, Y. Yarosh, F. Sun, and R. Lin, 2017: Reprocessed, bias-corrected CMORPH global high-resolution precipitation estimates from 1998. *J. Hydrometeorol.*, **18**, 1617–1641, <https://doi.org/10.1175/JHM-D-16-0168.1>.
- Yiou, P., E. Baert, and M. F. Loutre, 1996: Spectral analysis of climate data. *Surv. Geophys.*, **17**, 619–663, <https://doi.org/10.1007/BF01931784>.
- Zawadzki, I. I., 1973: Statistical properties of precipitation patterns. *J. Appl. Meteor. Climatol.*, **12**, 459–472, [https://doi.org/10.1175/1520-0450\(1973\)012<0459:SPOPP>2.0.CO;2](https://doi.org/10.1175/1520-0450(1973)012<0459:SPOPP>2.0.CO;2).
- Zhang, J., and Coauthors, 2016: Multi-Radar Multi-Sensor (MRMS) quantitative precipitation estimation: Initial operating capabilities. *Bull. Amer. Meteor. Soc.*, **97**, 621–638, <https://doi.org/10.1175/BAMS-D-14-00174.1>.